

# LLE Review

## Quarterly Report



January–March 1985

Laboratory for Laser Energetics  
College of Engineering and Applied Science  
University of Rochester  
250 East River Road  
Rochester, New York 14623-1299



# LLE Review

## Quarterly Report

*Editor:* H. Kim  
(716) 275-5850

January–March 1985

---

Laboratory for Laser Energetics  
College of Engineering and Applied Science  
University of Rochester  
250 East River Road  
Rochester, New York 14623-1299



This report was prepared as an account of work conducted by the Laboratory for Laser Energetics and sponsored by Empire State Electric Energy Research Corporation, General Electric Company, New York State Energy Research and Development Authority, Northeast Utilities Service Company, Ontario Hydro, Southern California Edison Company, The Standard Oil Company, University of Rochester, the U.S. Department of Energy, and other United States government agencies.

Neither the above named sponsors, nor any of their employees, makes any warranty, express or implied, or assumes any legal liability or responsibility for the accuracy, completeness, or usefulness of any information, apparatus, product, or process disclosed, or represents that its use would not infringe privately owned rights.

Reference herein to any specific commercial product, process, or service by trade name, mark, manufacturer, or otherwise, does not necessarily constitute or imply its endorsement, recommendation, or favoring by the United States Government or any agency thereof or any other sponsor.

Results reported in the LLE Review should not be taken as necessarily final results as they represent active research. The views and opinions of authors expressed herein do not necessarily state or reflect those of any of the above sponsoring entities.

## IN BRIEF

This volume of the LLE Review contains articles on completion of frequency conversion of the OMEGA system, recent progress in the laser-fusion effort, certain aspects of the LLE advanced technology program, and the National Laser Users Facility activities for January–March 1985.

The following are some highlights of the work described:

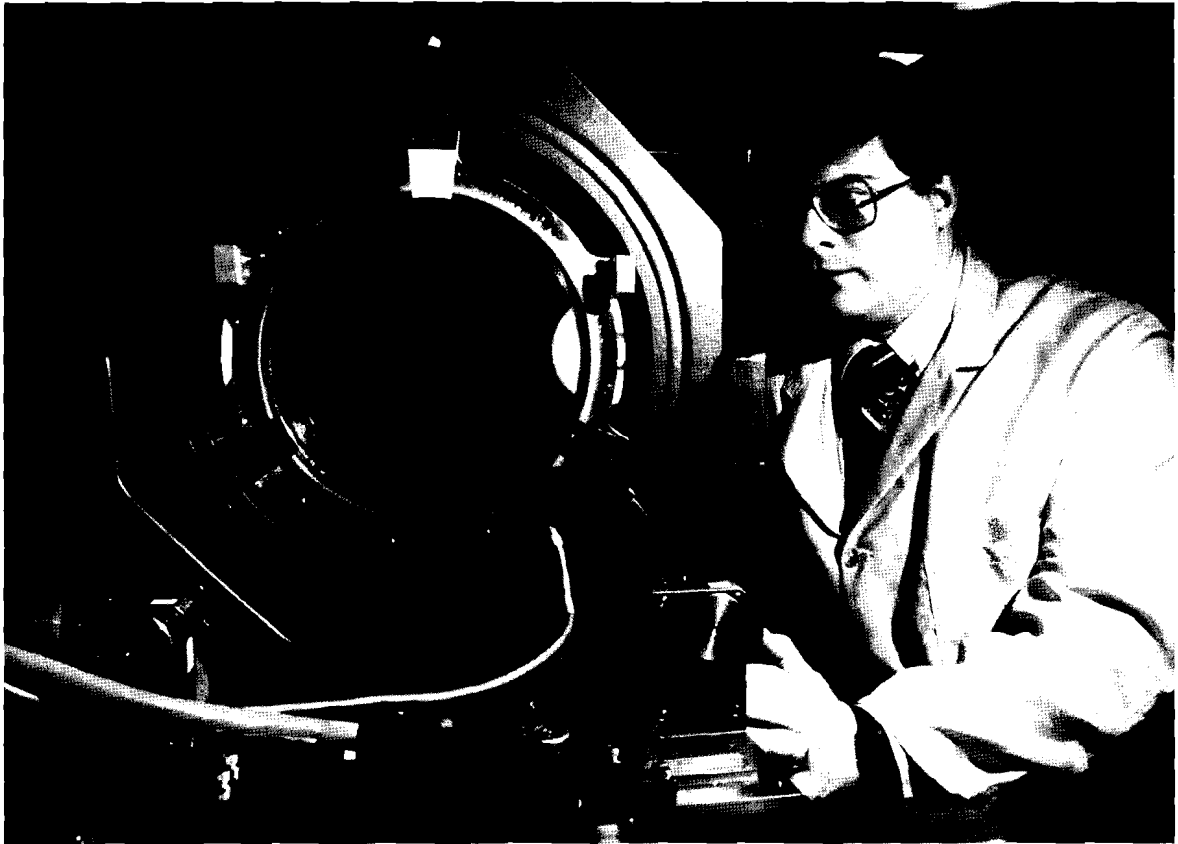
- The frequency conversion of all 24 beams of the OMEGA system from an IR to a UV output has been completed in this quarter. The converted OMEGA system produced energy exceeding 2 kJ.
- A method for measuring the temperature and the density-thickness product of an imploded target tamper has been developed. It relies on observing absorption lines of atomic species in a thin layer embedded within the target tamper.
- Measurements of soft x-ray emission from the plasmas of high-Z materials have been made to study x-ray conversion in a one-dimensional (1-D) spherical experiment and to determine whether there exist discrepancies between experimentally derived conversion efficiencies and those estimated from *LASNEX* numerical simulations.
- Recent thermal transport and target implosion experiments have been investigated using a non-Maxwellian electron distribution that simulates the effects of long mean-free-path electrons that

occur during heat transport. These effects are examined with an ionic rate-equation radiative-transfer analysis, in which atomic ionization and excitation rates are altered by a small population of electrons in a multi-keV "tail."

- A synchronously pumped, colliding-pulse, mode-locked dye laser that produces pulses of duration down to 70 fs has been developed. The system is based on a cw mode-locked Nd:YAG laser, so that kilohertz-repetition-rate, synchronous amplification is possible using a recently developed regenerative Nd:YAG amplifier. This oscillator-amplifier system produces ultrashort, microjoule pulses suitable for white-light continuum generation and sub-picosecond time-resolved spectroscopy.
- A dynamically loaded scratch tester has been developed that measures the relative adhesive strength of specimens within a given coating-substrate system. This tester minimizes the damaged regions of a coated part, yields real-time information in certain circumstances, and provides for the possibility of a limited amount of spatially resolved information.
- Electro-optic sampling is being used to characterize new classes of devices such as MESFET's and TEGFET's, which operate in the picosecond regime. This technique allows single devices to be investigated, yielding measurements essential for a complete understanding of these devices.

# CONTENTS

|   | <i>Page</i> |
|---|-------------|
| IN BRIEF .....  | iii         |
| CONTENTS .....  | v           |
| Section 1 LASER SYSTEM REPORT .....   | 49          |
| 1.A GDL Facility Report .....   | 49          |
| 1.B OMEGA Facility Report .....   | 50          |
| Section 2 PROGRESS IN LASER FUSION .....  | 51          |
| 2.A Absorption-Lines Measurement of Tamper $\rho\Delta R$<br>in Laser-Imploded Targets .....  | 51          |
| 2.B X-Ray Conversion Measurements<br>from High-Z Spherical Targets .....  | 60          |
| 2.C Effects of Non-Maxwellian Electron Populations<br>in Non-LTE Simulations of Laser-Plasma<br>Thermal Transport and Implosion Experiments ..... | 70          |
| Section 3 ADVANCED TECHNOLOGY DEVELOPMENTS .....  | 81          |
| 3.A Synchronously Pumped, Colliding-Pulse,<br>Mode-Locked Dye Laser .....   | 81          |
| 3.B Dynamically Loaded Scratch Tester for<br>Thin-Film Adhesion Measurements .....  | 85          |
| 3.C Characterization of Ultrafast Devices<br>Using Electro-Optic Sampling .....   | 94          |
| Section 4 NATIONAL LASER USERS FACILITY NEWS .....  | 99          |
| PUBLICATIONS AND CONFERENCE PRESENTATIONS   |             |



*William S. Beich, a technical associate in the Experimental Division, inspects one of the 24 frequency conversion cells recently installed on the OMEGA laser system for the generation of third harmonic light.*

# Section 1

## LASER SYSTEM REPORT

### 1.A GDL Facility Report

The glass development laser (GDL) system was deactivated in December 1984 for the installation of the Kuizenga oscillator, for the upgrade of the active mirror system, and for the activation of the frequency conversion system.

The schedule calls for the completion of the upgrade by early April, with testing of the synchronization of the two oscillators to occur in late March. A GDL operations summary for this period follows:

|  |           |
|--|-----------|
| GDL Pointing, Calibration, etc., Shots | 33        |
| Beta Tank Interaction Shots (IR)       | 33        |
| TOTAL                                  | <u>66</u> |

---

#### ACKNOWLEDGMENT

This work was supported by the U.S. Department of Energy Office of Inertial Fusion under agreement number DE-FC08-85DP40200 and by the Laser Fusion Feasibility Project at the Laboratory for Laser Energetics which has the following sponsors: Empire State Electric Energy Research Corporation, General Electric Company, New York State Energy Research and Development Authority, Northeast Utilities Service Company, Ontario Hydro, Southern California Edison Company, The Standard Oil Company, and University of Rochester. Such support does not imply endorsement of the content by any of the above parties.

## 1.B OMEGA Facility Report

During the second quarter of FY85 the wavelength conversion of all 24 beams of the OMEGA system from an IR (1054-nm) to a UV (351-nm) output was completed. The converted OMEGA system produced energy exceeding 2 kJ.

During this quarter, the conversion activities included assembly, test, and alignment of the conversion cells, and installation and alignment of the multi-wavelength energy-sensing system (MESS). In its first series of 24-beam shots on 8 February 1985, the frequency-tripled OMEGA system produced 900 J. After additional work on optimization of crystal alignment, beam transport measurements, near-field photography, focus lens characterization, and diagnostic activation, the energy was increased and reached 2087 J with 15% (rms) beam balance.

The 24-beam target experiments began in March 1985. OMEGA has demonstrated beam pointing accuracy and shot-to-shot stability of  $\pm 10 \mu\text{m}$  and beam-to-beam timing accuracy of  $\pm 3 \text{ ps}$ .

A summary of OMEGA operations during this quarter follows:

|                     |            |
|---------------------|------------|
| Software Test Shots | 31         |
| Driver Test Shots   | 45         |
| Beamline Test Shots | 49         |
| Target Shots        | <u>107</u> |
| TOTAL               | 232        |

---

### ACKNOWLEDGMENT

This work was supported by the U.S. Department of Energy Office of Inertial Fusion under agreement number DE-FC08-85DP40200 and by the Laser Fusion Feasibility Project at the Laboratory for Laser Energetics which has the following sponsors: Empire State Electric Energy Research Corporation, General Electric Company, New York State Energy Research and Development Authority, Northeast Utilities Service Company, Ontario Hydro, Southern California Edison Company, The Standard Oil Company, and University of Rochester. Such support does not imply endorsement of the content by any of the above parties.

## Section 2

# PROGRESS IN LASER FUSION

### 2.A Absorption-Lines Measurement of Tamper $\rho\Delta R$ in Laser-Imploded Targets

Laser-imploded targets, especially those imploded adiabatically, attain high temperatures in the compressed core. The imploded part of the surrounding tamper is considerably colder, especially if preheat is small. Under these conditions the continuous x-ray emission from the core undergoes absorption at wavelengths characteristic of atomic species in the tamper. The resulting absorption lines can yield information on the temperature ( $T_e$ ), density ( $\rho$ ), and the  $\rho\Delta R$  product of the tamper (density times thickness). Absorption can be particularly strong on resonance lines of the type 1s-2p in ions that have one or more vacancies in the  $n=2$  shell. The optimal choice of tamper species for this method is such that at the prevailing tamper temperature, ionization will remove some of the  $n=2$  electrons as well as all electrons of higher shells. For the present experiment, chlorine was a good choice, and, therefore, a KCl absorption layer was embedded within the tamper. Chlorine and potassium lines were observed and used to determine the conditions within the KCl layer and, by inference, within the rest of the tamper.

The experiment described here was performed on HELIOS, the eight-beam  $\text{CO}_2$  laser system at the Los Alamos National Laboratory (LANL). The results were analyzed jointly by scientists from LANL and LLE. The typical target in this experiment consisted of a 350- $\mu\text{m}$ -diameter glass shell of 0.8- $\mu\text{m}$  thickness, coated with a 0.5- $\mu\text{m}$  layer of KCl and then a 40- $\mu\text{m}$  layer of CH. The fill gas was 15 atm DT and 0.2 atm Ar (approximately 10% Ar by mass or by total number of electrons). The severe electron preheat was mitigated by choosing a very thick tamper,

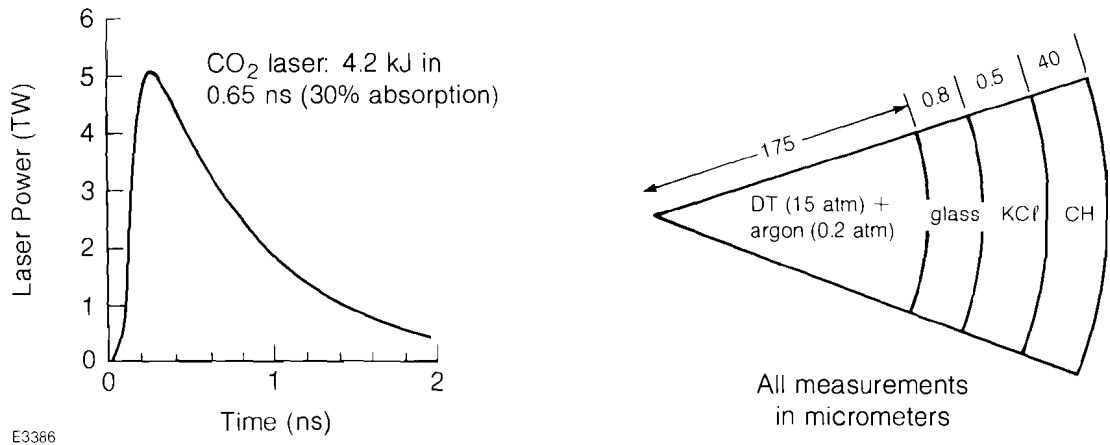
leading to modest preheat temperature. The tamper, after decompression from the preheat, recompresses to modest  $\rho$  and  $\rho\Delta R$  values. It is then that very distinct absorption lines (of Cl and K) appear in the spectrum. The Ar doping causes a relatively small perturbation on the target behavior but provides a signature for core temperature diagnosis. In addition, it contributes to the continuum intensity in the range 2.5 – 3.5 keV, which is required to see Cl and K absorption lines.

The method of using tamper absorption lines was previously reported by LLE<sup>1</sup> and by LANL.<sup>2</sup> The Rutherford Laboratory<sup>3</sup> reported on similar observations in planar targets. We discuss below the advantages of using absorption of higher-Z ions and analyze the results in much more detail than has been previously done. The values of  $T_e$  and  $\rho\Delta R$  derived from the experiment are in fair agreement with those predicted by the LASNEX laser-fusion code at LANL.

The absorption-lines method is similar to the method of neutron activation of tamper nuclei (such as <sup>28</sup>Si) except that here the temperature of the tamper can be determined as well. Furthermore, the method can be extended by using an external continuum source (in the backlighting mode). In this case, the parameters of the fuel can also be determined if a high-Z dopant is used. More important, the method can then be applied even if the core is too cold to emit x rays strongly.

We show in Fig. 22.1 the target and laser parameters used in this experiment. The very thick plastic coating is designed to yield a relatively low preheat temperature for the high total-preheat energy. For high enough total laser power, such a thick-shell target can still yield sufficiently high-core temperature to excite intense x-ray continuum around 3 keV (as well as 3- to 4-keV argon lines), which is a prerequisite for observing chlorine absorption lines. The relative position of the embedded KCl layer within the target is such that by the time of peak compression most or all of the CH layer (but none of the KCl layer) has been ablated. In order to relate the experimentally determined  $\rho\Delta R$  of

Fig. 22.1  
Target and laser parameters.



the  $K\ell$  layer to that of the total tamper, we need to rely on code calculations. To minimize dependence on such calculations, the glass shell should be much thinner than the  $K\ell$  layer. Alternatively, the  $\rho\Delta R$  of the compressed glass shell should be determined independently from absorption lines of silicon (or calcium), and this was not done here.

Fig. 22.2(a) shows an example of the spectrum recorded on film using a PET diffracting crystal. Clearly seen are Ar emission lines as well as  $C\ell$  and K absorption lines. The spatially resolving slit is too wide ( $40\ \mu\text{m}$ ) to show the size or structure of the core and is used here mainly to reduce detected emission from the target periphery, which does not participate in absorption-lines formation.

Fig. 22.2(b) shows a microdensitometer trace of the spatially resolved spectrum of Fig. 22.2(a). The background level lies just below the deepest absorption lines of  $C\ell$  and K. This means that at the frequencies of peak absorption most of the photons emitted by the core are absorbed — i.e., the optical depth there is significantly larger than 1. There are two recombination continua: one (below about  $5\ \text{\AA}$ ) due to recombination of  $\text{Si}^{+14}$  ions; the other (below about  $3.2\ \text{\AA}$ ) due to recombination of  $\text{Ar}^{+17}$  ions. The slope of either of these continua corresponds to a temperature of about 700 eV. The Ar line-intensity ratio  $(1s - 2p)/(1s^2 - 1s3p)$  can also be used to estimate the core temperature, and it yields  $\sim 600$  eV; this ratio is chosen to avoid the large opacity of the  $1s^2 - 1s2p$  line. The contrast between strong Ar emission lines and strong  $C\ell$  absorption lines vividly demonstrates a hot compressed core surrounded by a cooler shell. The tamper temperature deduced below is in fact much lower than this core temperature. The K lines appear less distinct than the  $C\ell$  lines only because they are absorbed by a weaker continuum, and are therefore not analyzed in detail here. However, the absorption fractions on these lines and therefore the deduced  $\rho\Delta R$  value are comparable to those of the  $C\ell$  lines.

Figure 22.3 shows in more detail the  $C\ell$  absorption structure. The identification of these lines was made by comparison with Hartree-Fock atomic structure calculations. As an example, the line marked B corresponds to transitions  $1s - 2p$  in boron-like chlorine ( $\text{Cl}^{+12}$ ) — i.e.,  $1s^2 2s^2 2p - 1s 2s^2 2p^2$ ; we likewise refer to other lines as the Be or the C feature, etc. For each configuration there can be several or many atomic states. For example, the He and Be features contain only one transition (ignoring a second, forbidden transition), whereas the B feature includes 14 transitions of which six are strong (i.e.,  $gf$  is larger than 0.1); the C feature contains 35 transitions of which 12 are strong. The broadening of the B, C, and especially the N, O features is to a large extent due to the splitting between the lines comprising each manifold (which are blended because of additional broadening). For example, the measured width of the B feature is about 14 eV, that of the Be feature 17 eV. The widths due to line splitting of, for instance, the B and N features are 6 and 12 eV, respectively. The Be feature has no such broadening.

The remaining broadening mechanisms affecting these features are instrumental broadening (about 3 eV) and Stark broadening. Additionally, the results below indicate that the optical depth at the peak of the

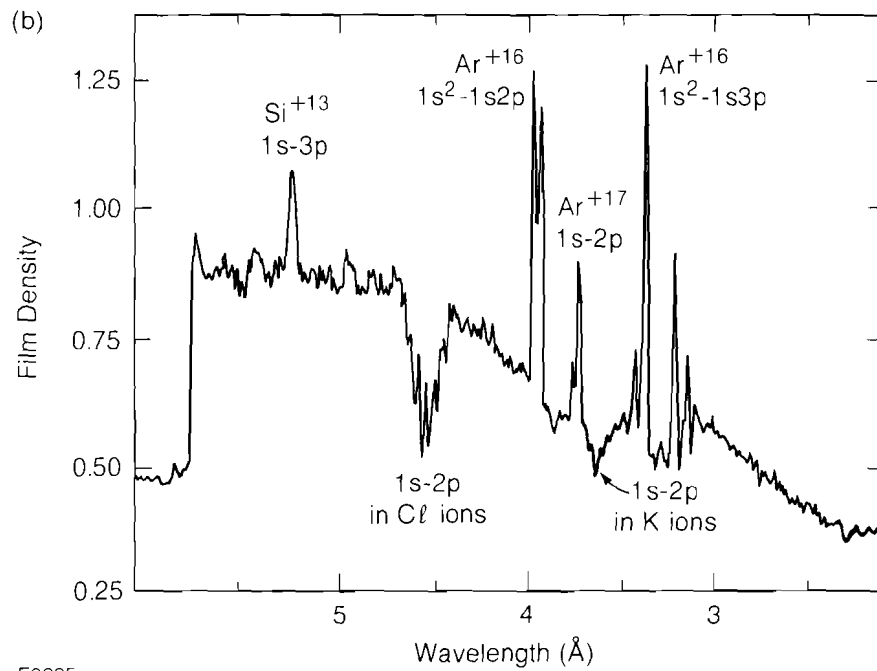
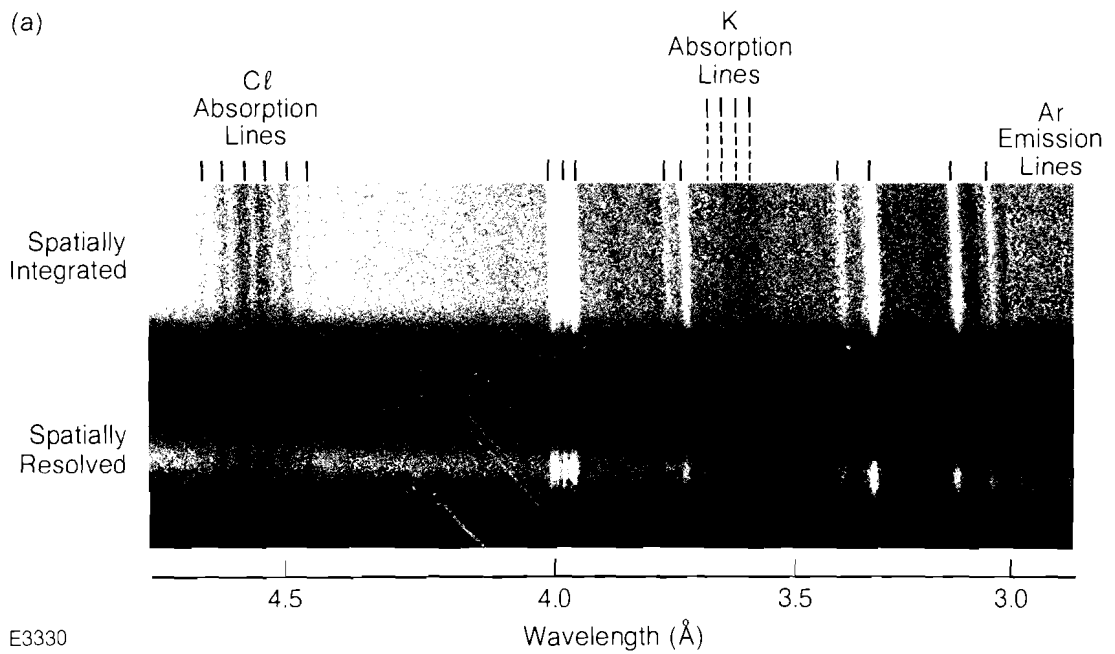
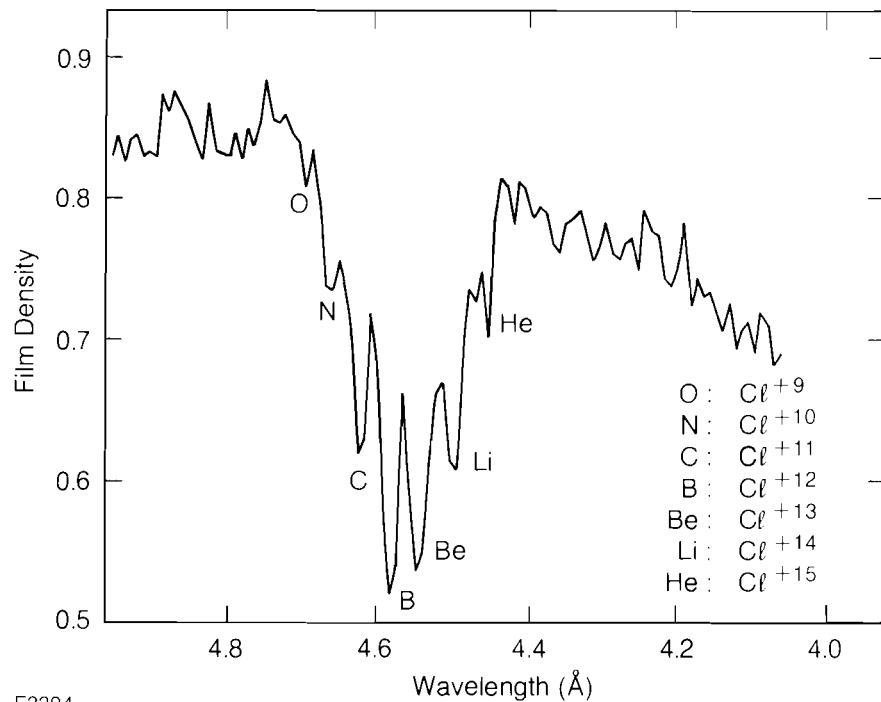


Fig. 22.2

(a) Film data obtained with a crystal x-ray spectrograph. White lines are emission lines of argon from the compressed core; black lines are absorption lines (of chlorine and potassium) from the tamper.  
 (b) Microdensitometer tracing of the spatially resolved spectrum of (a) showing line identification.



E3294

Fig. 22.3  
Detailed tracing of the chlorine absorption lines of Fig. 22.2(b). The feature marked B corresponds to the transition  $1s-2p$  in boron-like chlorine ( $Cl^{+12}$ ), etc.

Stark profile for these lines is much greater than 1 (the FWHM of the Stark profile of those lines is estimated to be less than 1 eV for electron density of the order  $10^{23} \text{cm}^{-3}$ ). Under these conditions the core radiation at the peak of the profile is depleted. The absorption line then broadens to a width such that the optical depth on the wings (e.g., the half-intensity points) is of the order 1. The line widths then depend both on  $\rho$  and  $\rho\Delta R$  and, especially because of the unavailability of Stark profile calculations for these lines, are not used here as diagnostic signatures.

The tamper temperature at the time of strong continuum emission from the core can be inferred from the intensity ratios of the absorption features. At higher tamper temperatures than here, features such as He or Li would dominate the absorption spectrum; at lower tamper temperatures it would be features such as N and O. The fact that the absorption features have a sharply peaked distribution of intensity is an indication that they are formed over a period when the temperature does not vary appreciably.

In order to estimate the tamper temperature from Fig. 22.3 we calculate the steady-state distribution of Cl charge states in a model that includes radiative, dielectronic, and three-body recombination, as well as ionization. The results (Fig. 22.4) show that this distribution depends primarily on the temperature and only slightly on the density in the range  $10^{23}$ – $10^{24} \text{cm}^{-3}$ . For this density range the deduced temperature by comparison to Fig. 22.3 is in the range 200–230 eV. The width

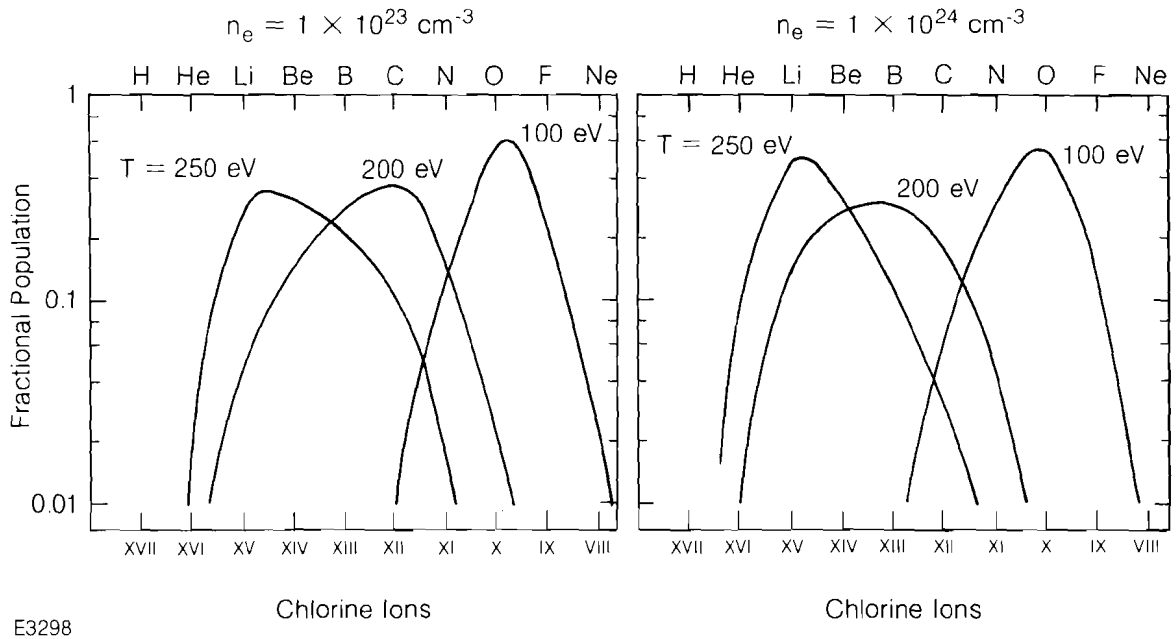


Fig. 22.4  
Atomic model calculations of chlorine charge state distribution at two densities. Smooth lines connect the calculated discrete points. Comparison of such curves to the spectrum of Fig. 22.3 is used to estimate the tamper temperature.

of the experimental and calculated distributions is comparable, indicating a temperature which does not vary appreciably over the time when the absorption features are formed. The determination of the tamper temperature, therefore, is not degraded as a consequence of not resolving the spectrum in time.

The determination of the tamper  $\rho\Delta R$  from the absorption lines is based on the cross section for photo-absorption on a spectral line of profile  $I(\nu)$ , normalized to total area of unity:

$$\sigma_\nu = (\pi e^2 / mc) f I(\nu), \tag{1}$$

where  $f$  is the absorption oscillator strength.

The attenuated intensity  $I(\nu)$  through a layer of thickness  $\Delta R$  and density  $\rho$  is related to the incident intensity  $I_0$  (assumed independent of frequency) through

$$I(\nu) = I_0 \exp(-\sigma_\nu N_i \Delta R) = I_0 \exp(-\alpha \rho \Delta R / M_i), \tag{2}$$

where  $\alpha$  is the fraction of all ions of type  $i$ , which are in the ground state and whose density is  $N_i$ . For the case of absorption lines  $\alpha$  is inevitably very nearly equal to 1 because the temperature where they are formed is much smaller than the excitation energy of these lines. For some of these chlorine ions the ground configuration consists of several closely spaced states, and their total population densities are added; this means that the  $f$  value in Eq. (1) has to be averaged over the lower-state levels as well as summed over the upper-state levels. For example, the Be ion

has one ground state ( $^1S_0$ ); the B ions, two ( $^2P_{1/2}$ ,  $^2P_{3/2}$ ); and the C ion, five ( $^1D_2$ ,  $^1S_0$ ,  $^3P_2$ ,  $^3P_1$ ,  $^3P_0$ ).

The  $\rho\Delta R$  can then be derived from the equation

$$\rho\Delta R = (M_i/\sigma\alpha) \int \ell_n (I_0/I_\nu) d\nu. \quad (3)$$

The integral is effectively over the line profile because the integrand vanishes far from line center. In the approximation that the film density in Fig. 22.3 is proportional to  $\ell_n (I)$ , this integral is simply the area enclosed within the absorption line. For each absorption line, this equation yields the partial  $\rho\Delta R$  value related to the corresponding ion. The total  $\rho\Delta R$  of the  $KCl$  layer is given by

$$\rho\Delta R (KCl) = 2.2 \rho\Delta R (Cl) = 2.2 \sum_i \rho\Delta R (Cl_i), \quad (4)$$

where the summation is over the absorption-lines manifold in Fig. 22.3.

It is important to note that only the integral over the line profile is required for the determination of  $\rho\Delta R$ , so that the line profile need not be known. Also, the deconvolution required to separate the contribution of the partly overlapping absorption lines is not critical. For example, if the  $f$  values of these absorption lines were the same, we would only need to integrate the entire absorption manifold of Fig. 22.3 without any deconvolution.

Applying the procedure described here to the absorption lines of Fig. 22.3, following conversion from film density to intensity, overlapping lines deconvolution, and integration, we derive a value of

$$\rho\Delta R = 5.3 \times 10^{-4} \text{ g/cm}^2$$

for the  $KCl$  layer. The main sources of error in deriving the  $\rho\Delta R$  value come from the determination of the area enclosed within the absorption lines and from uncertainties in film calibration curves. These errors are estimated to be  $\pm 20\%$ . An additional error in time-integrated spectra can be caused by core emission of continuum, prior to the time the absorption lines are formed. This can occur when the core starts to compress and heat up, but the shell still moves inward and is too cold to absorb on  $1s-2p$  transitions because there are no vacancies in the  $n=2$  electronic shell. This error should in general be small because of the logarithmic dependence of the derived  $\rho\Delta R$  value on the measured intensity [Eq. (3)]; it always results in underestimating the correct  $\rho\Delta R$  value. If at least one of the absorption lines approaches the background level [as is the case for both the  $Cl$  and  $K$  groups in Fig. 22.2(b)], then this effect is unimportant and temporally resolving the spectrum is not essential.

The *LASNEX* laser-fusion code in a one-dimensional mode was used to simulate these experiments. In Fig. 22.5, we show the calculated time history of the electron temperature, averaged over each target layer. At the time of peak core temperature, which should be about the time of peak core emission of continuum, the temperature in the  $KCl$  layer is

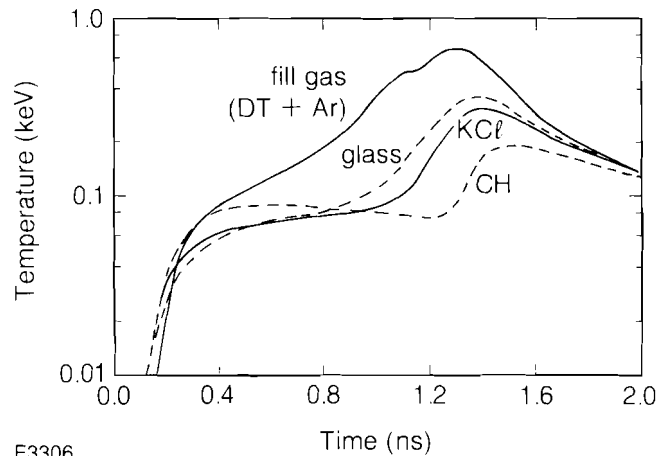


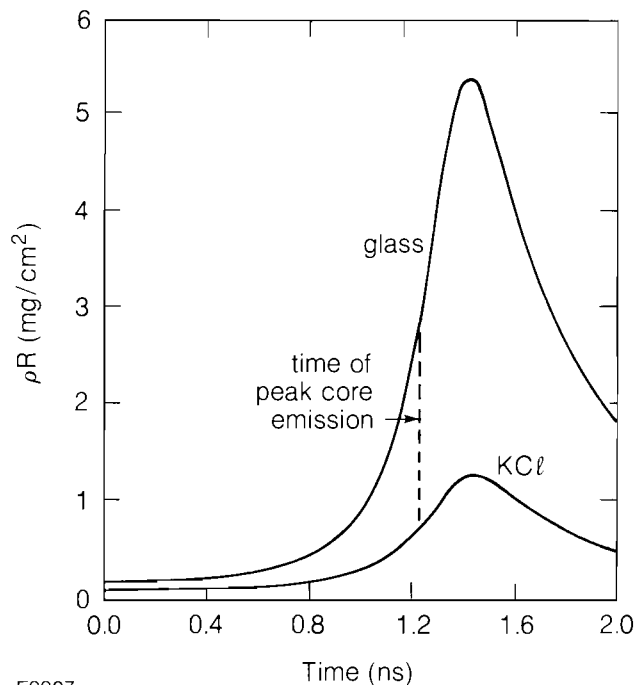
Fig. 22.5  
LASNEX-calculated temperature history  
averaged over each of four target layers.

predicted to be 250 eV, in good agreement with the range 200–230 eV determined from the experiment. It should be pointed out that the predicted preheat temperature is only about 80 eV. The rise in tamper temperature, at about 1.1 ns, is due to heat flowing outward from the hot fill gas as well as due to the recompression of the expanded tamper. As is evident by comparing Figs. 22.1 and 22.5, the compression occurs much after the peak of the laser pulse.

Figure 22.6 shows the time history of the  $\rho\Delta R$  of both the glass and KCl layers. At the time of peak core temperature, assumed to be the time of peak core emission, the  $\rho\Delta R$  of the KCl layer is

$$6.8 \times 10^{-4} \text{ g/cm}^2,$$

in rough agreement with the experimentally derived value. We can infer from here by using the computational results of Fig. 22.6 that the total  $\rho\Delta R$  of the tamper at that time was about  $3.4 \times 10^{-3} \text{ g/cm}^2$ . An important conclusion from Figs. 22.5 and 22.6 is that this method is useful in determining the peak tamper  $\rho\Delta R$  only if the implosion is well timed so that the peaks in core temperature and in tamper  $\rho\Delta R$  occur at the same time. For future high-performance target implosions (such as expected with short-wavelength lasers), the target tamper in similar experiments will have to consist of a very thin signature layer in a low-Z (plastic) shell. This is because a high- $\rho\Delta R$ , compressed shell can absorb strongly even photons of nonresonant frequency (by the photoelectric, or bound-free, mechanism) so that no absorption lines would appear in the spectrum. This problem will be especially severe in such targets because the tamper temperature is expected to be lower, which will necessitate choosing a lower-Z signature layer. Otherwise, no electrons of the  $n=2$  shell will be ionized. Lower-Z ions have transitions of longer wavelength where the absorption is even more severe. To counter such excessive absorption, the targets should have a thin enough signature layer, located deep enough in a low-Z tamper, so that it does not undergo ablation or expansion before peak compression of



E3307

Fig. 22.6  
LASNEX-calculated  $\rho\Delta R$  history for the two  
tamper layers.

the core. The choice of chlorine for the present experiment was appropriate because for higher-Z species (even for potassium) the lower-continuum intensity limits the precision; on the other hand, for much lower-Z species, the glass-shell absorption is severe even in the present experiment. A more detailed determination of tamper parameters can be obtained by embedding several signature layers within the inner part of the tamper with deeper layers having a higher nuclear charge-Z species.

#### ACKNOWLEDGMENT

This work was supported by the U.S. Department of Energy Office of Inertial Fusion under agreement number DE-FC08-85DP40200, by the Los Alamos National Laboratory, and by the Laser Fusion Feasibility Project at the Laboratory for Laser Energetics which has the following sponsors: Empire State Electric Energy Research Corporation, General Electric Company, New York State Energy Research and Development Authority, Northeast Utilities Service Company, Ontario Hydro, Southern California Edison Company, The Standard Oil Company, and University of Rochester. Such support does not imply endorsement of the content by any of the above parties.

#### REFERENCES

1. B. Yaakobi, R. L. McCrory, S. Skupsky, J. A. Delettrez, P. Bourke, H. Deckman, C. F. Hooper, and J. M. Soures, *Opt. Commun.* **34**, 213 (1980).
2. A. Hauer, in *Spectral Line Shapes*, edited by B. Wende (Springer, Berlin, 1981).
3. D. K. Bradely, J. D. Hares, and J. D. Kilkenny, Rutherford-Appleton Laboratory Annual Report RL-83-043, p. 5.4.

## 2.B X-Ray Conversion Measurements from High-Z Spherical Targets

Quantitative measurements of the x-ray emission from laser-produced plasmas have been a subject of considerable interest since the early 1970s.<sup>1</sup> With the fabrication of large, in some cases multibeam, high-power laser systems, much work has been performed on the analysis of x-ray emission from laser-produced plasmas of high-atomic-number materials.<sup>2</sup> Measurements of soft x-ray emission from the plasmas of high-Z materials, particularly Au targets, are not only of considerable interest for inertial confinement fusion applications but are also relevant to a number of potential applications of laser-produced x rays. For these reasons, there is a need for the quantitative understanding, through hydrodynamic and atomic physics numerical codes, of soft x-ray production from laser-irradiated solid targets. This is particularly the case for interaction experiments with high-power, short-wavelength laser radiation. Such experiments exhibit not only high overall coupling efficiency but also produce, for high-Z targets, greater soft x-ray emission. However, experiments to date have all been performed with planar targets, irradiated by single or nonuniform multiple-laser beams. A number of studies have been performed at Lawrence Livermore National Laboratory (LLNL) with the ARGUS<sup>3</sup> and NOVETTE<sup>4</sup> laser systems to compare the experimentally determined conversion efficiencies to x rays and those estimated from numerical simulations performed with the laser-fusion hydrodynamic code *LASNEX*. At low intensities ( $< 8 \times 10^{13}$  W/cm<sup>2</sup>), the measured x-ray conversion efficiency<sup>3</sup> is lower than that predicted by *LASNEX*.

In a collaborative set of experiments between Los Alamos National Laboratory (LANL) and the Laboratory for Laser Energetics (LLE), the first detailed investigation of x-ray conversion from high-Z (Au) spherical targets was made during the summer of 1984.<sup>5</sup> This investigation used a symmetric (cubic) set of six UV beams from the 24-beam OMEGA laser system.<sup>6</sup> The primary motivation behind these investigations was the study of x-ray conversion in a nearly 1-D spherical experiment to determine if previously observed discrepancies still exist. To this aim, detailed measurements were made in one dimension of the energy flow, coronal plasma conditions, and emission characteristics of x rays. From these studies it was hoped to identify modifications to the *LASNEX* model required to correctly match experimental observables.

These studies were made with an extensive array of x-ray diagnostics, fielded jointly by LLE and LANL, including (a) a four-channel, absolutely calibrated x-ray diode spectrometer, (b) a 15-channel diode/scintillator-photomultiplier x-ray continuum emission spectrometer, (c) x-ray crystal and grazing incidence XUV spectrographs, (d) a time-resolved (streak) x-ray grating spectrograph, (e) a time-resolved (streak) curved x-ray crystal spectrograph (SPEAX), (f) x-ray pinhole camera and microscope imaging, and (g) time-resolved x-ray streak photography. In addition, coronal plasma conditions were monitored with plasma calorimeters, charged collectors, harmonic emission diodes, and spectrographic

measurements of the  $\omega/2$  harmonic emission. In the experiments, six 351-nm beams of OMEGA irradiated Au-coated, solid CH targets with intensity range at two intensities,  $4 \times 10^{13} \text{ W/cm}^2$  and  $4 \times 10^{14} \text{ W/cm}^2$ . For OMEGA irradiation conditions, a sharp transition occurs between the low- and high-intensity cases; in the latter case, short scale lengths produce higher coronal temperatures, a higher ionization state, and the consequential emission of M-line radiation. A detailed set of measurements were made with targets having various thicknesses of Au to investigate the progress of the ionization front, and the burn-through to the underlying low-Z material. All these experiments were performed with the six UV beams focused tangentially on spherical targets of 600- $\mu\text{m}$  or 200- $\mu\text{m}$  diameter, to provide the maximum level of irradiation uniformity with total energies of the order of 250 J in 600-ps (FWHM) pulses.

Absolute x-ray flux measurements were made with four calibrated soft x-ray diodes, each sampling separate regions of the x-ray emission between 0.1 and 1 keV through the use of a number of thin metallic and plastic filters. The overall x-ray conversion ( $\sim 60\%$ ), shown in Fig. 22.7, indicates little apparent intensity dependence. At the lower

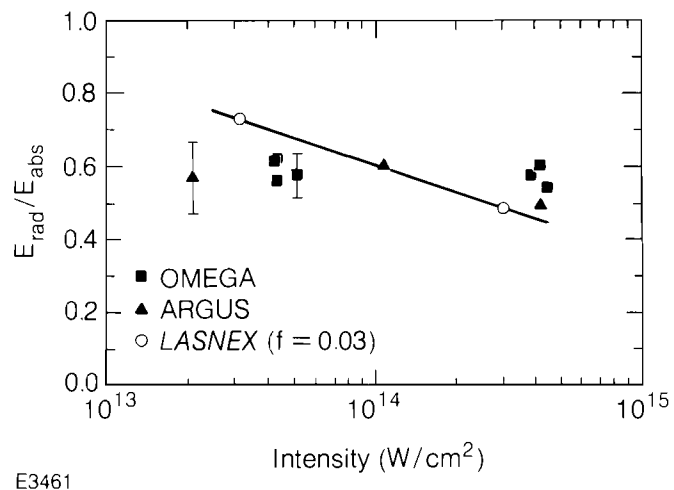


Fig. 22.7  
X-ray conversion as a function of incident intensity.

intensity ( $\sim 4 \times 10^{13} \text{ W/cm}^2$ ), the conversion of the incident laser energy into x rays was 0.52, this value dropping to 0.44 at intensities of  $\sim 4 \times 10^{14} \text{ W/cm}^2$ . This observation is consistent with the previous planar target (ARGUS) data but deviates, particularly at low intensities, from the predictions of a flux-limited ( $f = 0.03$ ) LASNEX model. This difference between simulations and experiment at low intensities requires further study; in a future series of measurements, x-ray conversion at lower intensities and at higher intensities in spherical geometry will be measured. In studies of the x-ray conversion as a function of the Au thickness, LASNEX in general predicted well the observed falloff in x-ray conversion for thin Au layers at both intensities. Experimental data are given in Fig. 22.8. As shown in Fig. 22.9, the falloff in x-ray conversion

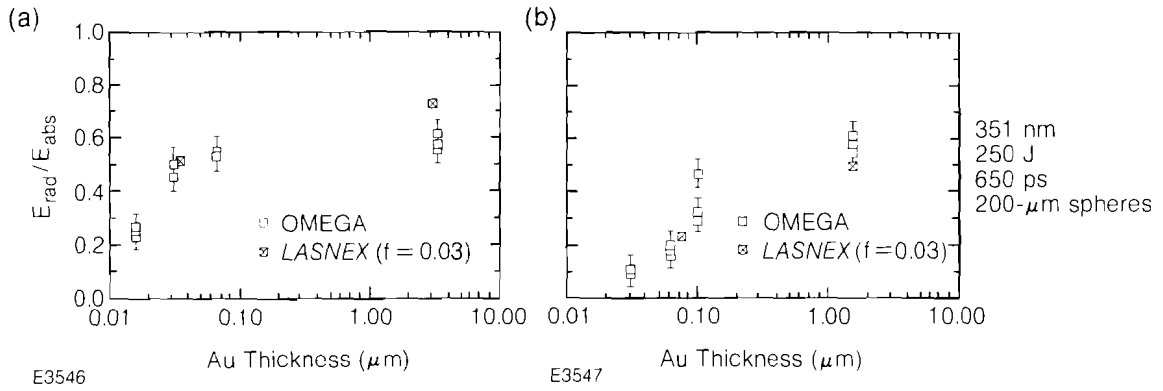


Fig. 22.8  
Variation in x-ray conversion as a function of Au thickness for (a)  $4 \times 10^{14} W/cm^2$  and (b)  $4 \times 10^{13} W/cm^2$ .

occurred at a thickness at which the conversion efficiency of half-harmonic emission increased by an order of magnitude, and where the x-ray bremsstrahlung yield from superthermal electrons, measured with the K-edge spectrometer, increased several fold. This indicates that under conditions where burn-through of the gold occurs during the laser pulse, the underdense scale length changes to permit the onset of the  $2 \omega_p$  instability at  $n_c/4$ , resulting in an increase in  $\omega/2$  emission and superthermal electrons.<sup>7</sup>

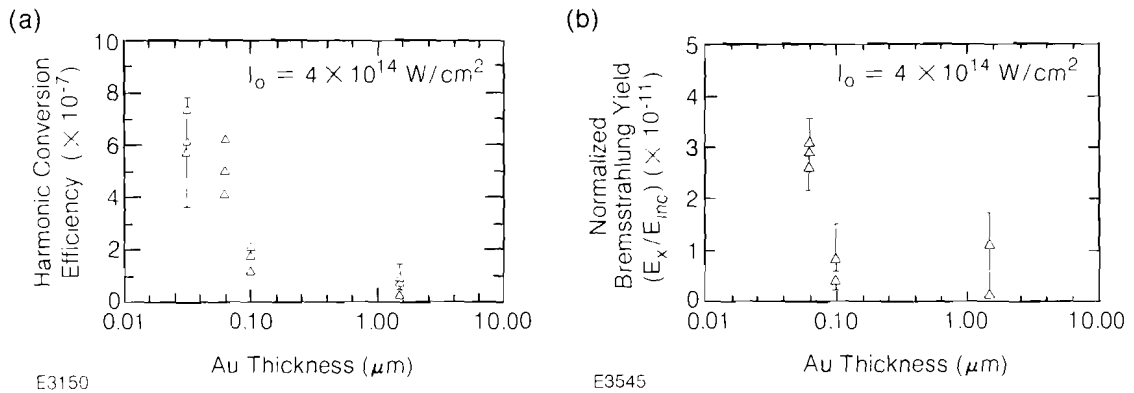
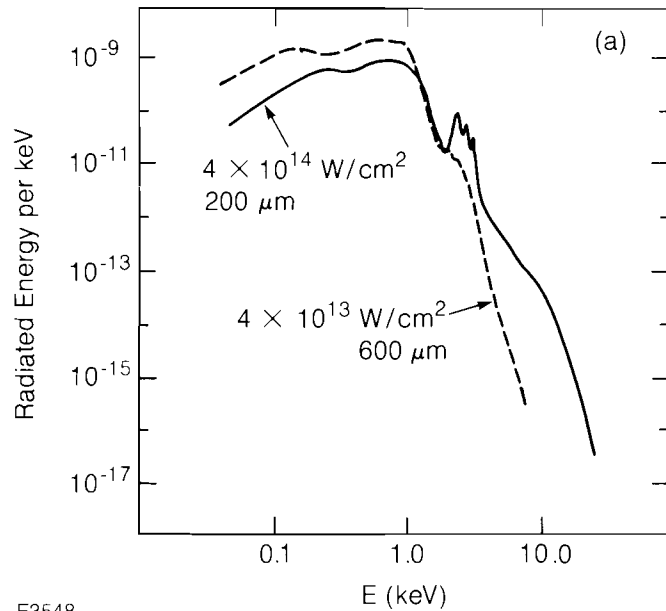


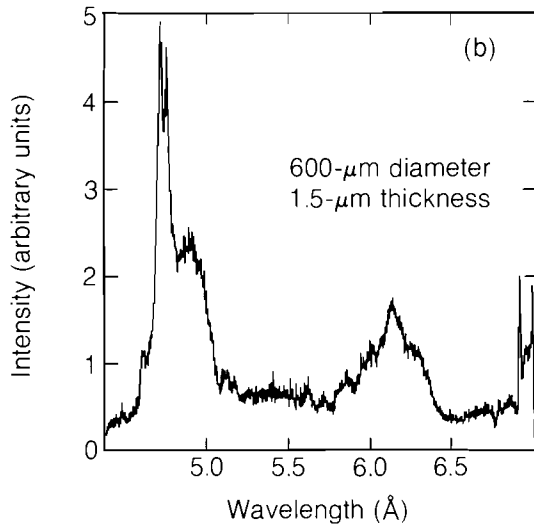
Fig. 22.9  
Change in the level of  $\omega/2$  harmonic emission (a), and superhot bremsstrahlung x-ray emission (b), as the thickness of Au is decreased below the burn-through thickness.

A parametric study of M-line emission from Au targets was made using time-integrated and time-resolved spectrographic instrumentations. At the higher intensity of  $4 \times 10^{14} W/cm^2$ , LASNEX predicts, as shown in Fig. 22.10(a), the onset of strong M-line emission due to the creation of a higher temperature. Experimentally, the LASNEX prediction was confirmed, as shown in Figs. 22.10(b) and 22.10(c). These figures show the lack of any strong M-line emission at  $4 \times 10^{13} W/cm^2$  and its strong appearance in the 5- to 6- $\text{\AA}$  region at  $4 \times 10^{14} W/cm^2$ . At the higher intensities, the onset of M-line emission was also found to be strongly dependent on the thickness of Au. For the smallest thicknesses used (0.06  $\mu m$ ), the level of M-line emission was small.

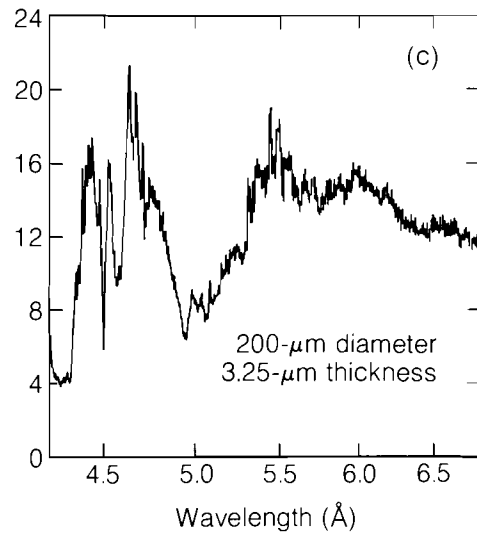
Fig. 22.10  
 Onset of strong M-line emission in going from  $4 \times 10^{13}$  W/cm<sup>2</sup> as predicted by LASNEX (a) and as found in experiment at  $4 \times 10^{13}$  W/cm<sup>2</sup> (b) and  $4 \times 10^{14}$  W/cm<sup>2</sup> (c).



E3548



E3187



Time-resolved x-ray spectral measurements were made with two devices, a transmission-grating streak spectrograph,<sup>8</sup> sensitive in the 1- to 30-Å region, and an elliptical crystal streak spectrograph,<sup>9</sup> sensitive in the 5.2- to 7.1-Å region. The former instrument had a broad spectral range but limited resolution ( $\lambda/\Delta\lambda \sim 100$ ), while the latter had high resolution ( $\lambda/\Delta\lambda \sim 1000$ ) but a limited spectral range, centrally located in the band of M-lines. While the M-line emission appears as a broadband centered in the 5- to 6-Å region in the transmission-grating spectrograph, details of the M-lines can be seen from the crystal streak spectrograph. Detailed convolution of data such as shown in Fig. 22.11 can render considerable information about the temporal evolution of the

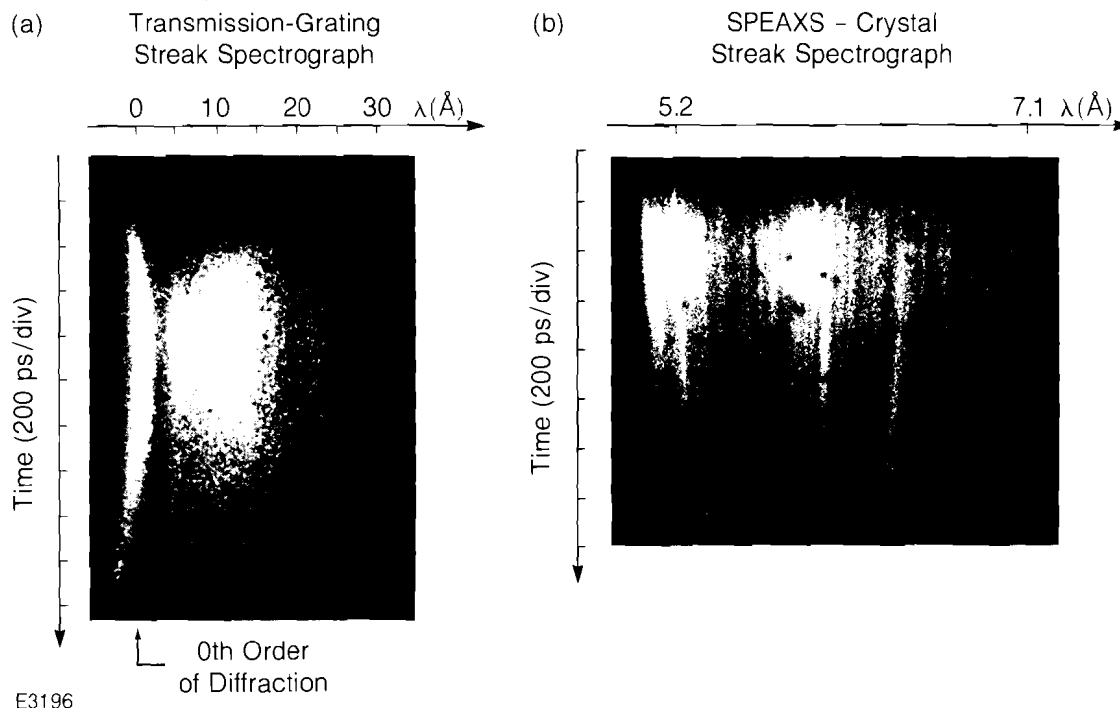


Fig. 22.11

Typical time-resolved spectra obtained from Au targets and the transmission-grating streak spectrograph (a), and the crystal streak spectrograph, SPEAXS (b).

M-line emission. Figure 22.12(a) shows, for example, the duration of the M-line emission from 4.8–6.9 Å, deduced from the transmission-grating spectrograph, for the case of a 0.062- $\mu\text{m}$ , thick-coated Au target at high intensity. The duration of the M-line emission is considerably shorter than the 600-ps duration (FWHM) of the laser pulse. This should be compared with the *LASNEX* prediction of the duration of the M-line emission under these conditions, shown in Fig. 22.12(b). There is reasonably close agreement between simulation and experiment. In general, *LASNEX* models well the duration of the M-line emission under various irradiation conditions, with the exception that in the case of very thin Au target layers, at high intensities, the duration of the M-line emission is truncated less sharply than the code would predict. This may well be a consequence of the effects of irradiation nonuniformities on the surface of the target, a subject which will be discussed in more detail.

The streak x-ray crystal spectrograph, with its high resolution, can provide detailed information on the time evolution of M-lines. Figure 22.13 shows time-resolved spectra of the M-line emission for targets irradiated at high intensity ( $4 \times 10^{14}$  W/cm<sup>2</sup>) for different thicknesses of Au-coated CH targets. The duration of the individual M-lines is reduced as the thickness of Au is reduced. The wavelength of these specific M-lines, not well known at present, is calibrated by fiducial Si lines emanating from portions of the glass stalk used to support the target. Reduction of this data can render extremely detailed information on the time history of all M-lines observed.

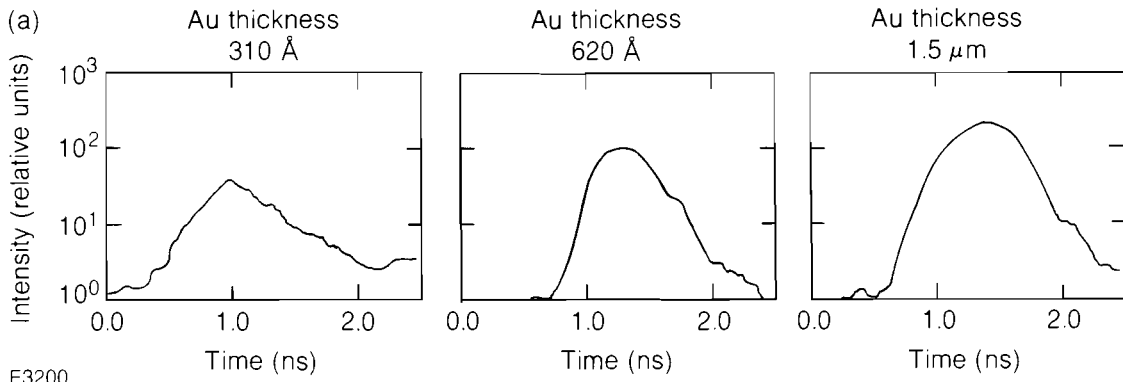
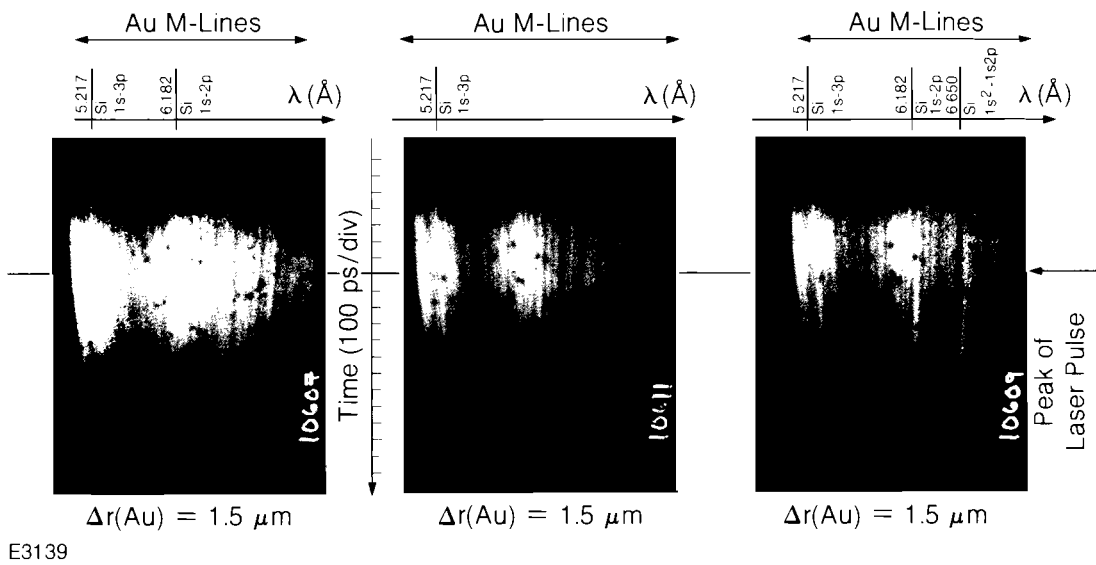


Fig. 22.12  
Time history of M-line emission deduced from x-ray grating streak spectrograph (a), for a 620-Å-thick Au layer, irradiated at  $4 \times 10^{14}$  W/cm<sup>2</sup>, compared to the prediction from LASNEX (b).

Fig. 22.13  
Details of the temporal evolution of the M-line emission, produced by the SPEAXS instrument, for various thicknesses of Au, irradiated at  $4 \times 10^{14}$  W/cm<sup>2</sup>. Fiducial Si lines, emanating from portions of the glass stalk evaporated by the laser, are also observable.



Detailed diagnosis of x-ray images in these experiments was performed to evaluate the level to which uniform irradiation of the target could be depended upon, and to identify nonuniformities in the surface x-ray emission of the target. Several different instruments were used. Figure 22.14 shows typical x-ray images of the target obtained with three different instruments — a pinhole camera filter combination selecting x-ray emission in the sub-keV range, a second pinhole camera/filter system producing images of 1.0-keV x-ray emission, and a Kirkpatrick-Baez microscope, which produces x-ray images in the 3-keV x-ray emission. Analysis of these x-ray images, as for example

- Au-coated CH spherical targets, 600- $\mu\text{m}$  diameter
- Au thickness 3.5  $\mu\text{m}$
- Incident intensity  $\sim 4 \times 10^{13} \text{ W/cm}^2$

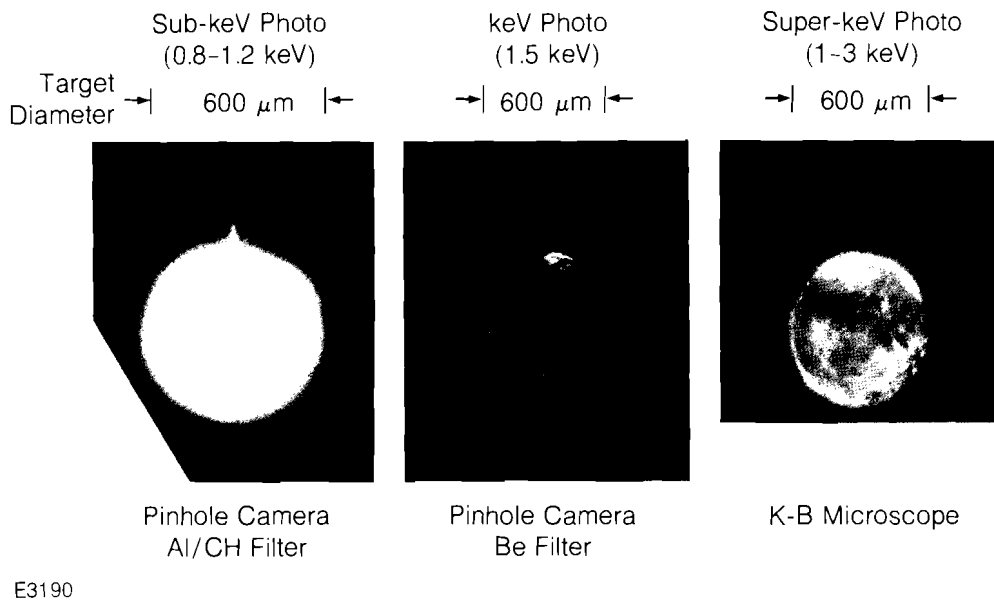


Fig. 22.14  
X-ray analysis in different x-ray regions, detailed with two pinhole cameras and a Kirkpatrick-Baez microscope.

shown in Fig. 22.15(a), indicates that the variation in x-ray emission across the surface of the target in regions of the image where limb brightening is not a factor can be at least a factor of 2. The level of irradiation uniformity incident on the target, for six beam irradiation conditions, is shown in Fig. 22.15(b).<sup>10</sup> Disregarding the small intense hot spots in the irradiation distribution, it can be seen that the overall variation in intensity in long spatial frequencies is approximately a factor of 2; qualitatively, this is comparable to the x-ray photographic data. Assuming the same level of uniformity presently existing in each individual beam, it is expected that with 24-beam irradiation at the same irradiation and focusing conditions, the overall level of irradiation uniformity on the surface of the sphere will improve by at least a factor of 6.

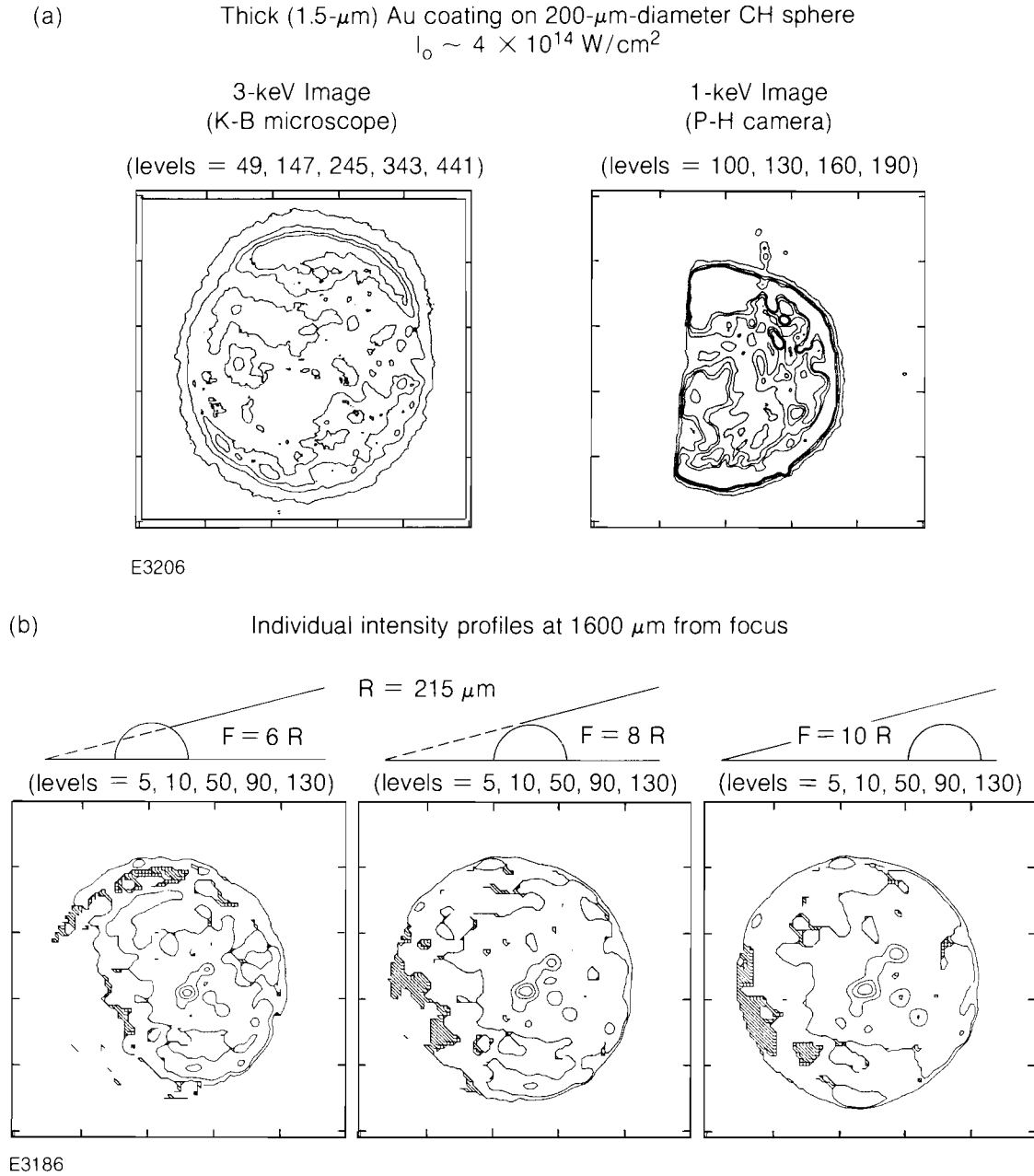
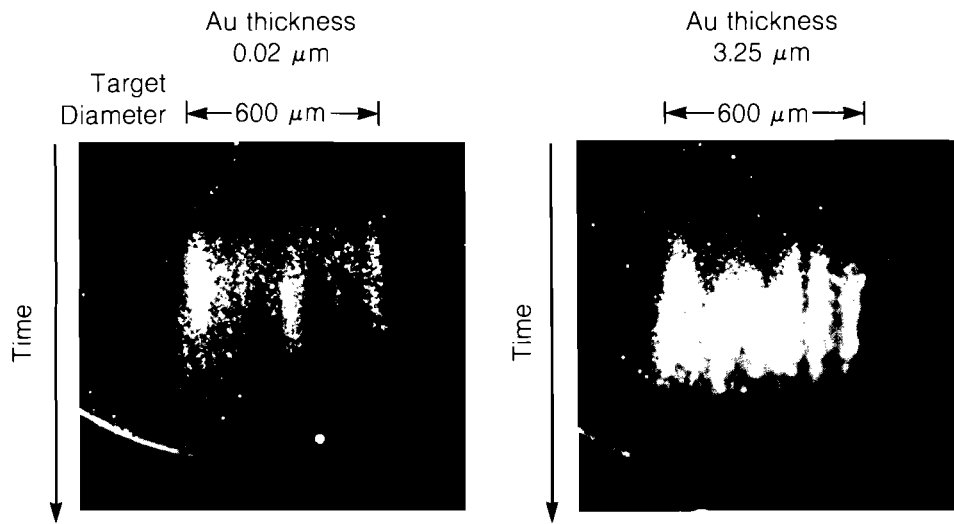


Fig. 22.15  
 Nonuniformities evident in x-ray emission on the surface of the target (a), compared to estimated irradiation nonuniformities deduced from a detailed knowledge of the intensity distributions of each beam, mapped onto the surface of a sphere (b).

Time-resolved photographic studies of the emission from the target were made with a streak x-ray pinhole camera system. Some typical data, taken at low irradiation conditions ( $4 \times 10^{13} \text{ W/cm}^2$ ), are shown in Fig. 22.16. For both thick and thin layers of gold, spatial structure is clearly evident in the x-ray emission. The level to which this spatial structure in the x-ray emission alters the 1-D description used in the LASNEX simulation is under detailed study.



E3193

Fig. 22.16  
Time-resolved x-ray photography of Au-coated targets at an intensity of  $4 \times 10^{13}$  W/cm<sup>2</sup>.

In summary, this comprehensive characterization of x-ray conversion from spherical high-Z (Au) targets with short-wavelength irradiation has produced much interesting information. Detailed measurements of the dependence of the x-ray conversion efficiency on laser irradiance has confirmed a previously observed intensity dependence, which is smaller than that predicted by the *LASNEX* hydrodynamic code. The deployment of a large array of time-resolved, space-resolved, and time-integrated x-ray instrumentation has rendered an extensive investigation of the Au M-line emission with high spectral, spatial, and temporal resolution. The data from several diagnostics specifically deployed to characterize coronal plasma conditions compare well to code predictions. Finally, although there is, in general, close agreement between the experimental data and the 1-D *LASNEX* predictions, the effects of irradiation nonuniformities across the surface of the target, produced with only six-beam irradiation conditions, cannot be ignored. The level of irradiation uniformity has been assessed from detailed knowledge of beam characteristics and through x-ray microscopy. It is anticipated that in future experiments, performed with 24 beams, the effects of microscopic nonuniformities across the surface of the target will be reduced compared to the six-beam experiments.

#### ACKNOWLEDGMENT

This work was supported by the U.S. Department of Energy Office of Inertial Fusion under agreement number DE-FC08-85DP40200 and in part by Los Alamos National Laboratory under subcontract 9-XR4-P1019-1, effective 1 May 1984.

## REFERENCES

1. D. J. Nagel *et al.*, *Phys. Rev. Lett.* **33**, 743 (1974).
2. B. Yaakobi, T. Boehly, P. Bourke, Y. Conturie, R. S. Craxton, J. Delettrez, J. M. Forsyth, R. D. Frankel, L. M. Goldman, R. L. McCrory, M. C. Richardson, W. Seka, D. Shvarts, and J. M. Soures, *Opt. Comm.* **39**, 175 (1981).
3. W. C. Mead *et al.*, *Phys. Rev. Lett.* **47**, 1289 (1981).
4. R. L. Kauffman *et al.*, *Bull. Am. Phys. Soc.* **29**, 1183, paper 1R1 (1984).
5. P. D. Goldstone, R. H. Day, G. Eden, F. Ameduri, W. C. Mead, S. R. Goldman, M. C. Richardson, R. L. Keck, W. Seka, G. Pien, J. M. Soures, and R. L. McCrory, *Bull. Am. Phys. Soc.* **29**, 1318, paper 6E5 (1984); R. S. Marjoribanks, G. Stradling, M. C. Richardson, A. Hauer, O. Barnouin, B. Yaakobi, S. A. Letzring, and P. D. Goldstone, *ibid.* **29**, 1318, paper 6E6 (1984); S. A. Letzring, M. C. Richardson, P. D. Goldstone, G. Gregory, and G. Eden, *ibid.* **29**, 1318, paper 6E7 (1984); S. R. Goldman, W. C. Mead, P. D. Goldstone, and M. C. Richardson, *ibid.* **29**, 1319, paper 6E8 (1984).
6. LLE Review **17**, 3 (1983); J. M. Soures, R. J. Hutchison, S. D. Jacobs, L. D. Lund, R. L. McCrory, and M. C. Richardson, in Proceedings of the 10th Symposium on Fusion Engineering, Philadelphia, 1983.
7. W. Seka, B. B. Afeyan, R. Boni, L. M. Goldman, R. W. Short, K. Tanaka, and T. W. Johnson (submitted for publication).
8. M. C. Richardson, R. S. Marjoribanks, S. A. Letzring, J. M. Forsyth, and D. M. Villeneuve, *IEEE J. Quantum Electron.* **QE-19**, 1861 (1983).
9. B. L. Henke and P. A. Jaanimagi, *Bull. Am. Phys. Soc.* **29**, 1388, paper 8R8 (1984).
10. LLE Review **20**, 150 (1984).

## 2.C Effects of Non-Maxwellian Electron Populations in Non-LTE Simulations of Laser-Plasma Thermal Transport and Implosion Experiments

Spectrally and spatially resolved x rays are widely used diagnostics for high-temperature plasmas in laser-driven experiments. The relatively small time scales and small optical depths that occur often require a non-LTE (local thermodynamic equilibrium) analysis of atomic phenomena, and the relatively long mean free path of the most energetic electrons can make non-Maxwellian electron energy distributions relevant to the interpretation of the diagnostic signals. Just as deviations from a Planck photon spectrum occur in radiative transfer problems when photon optical depths are comparable to configurational scale lengths, small deviations from Maxwell-Boltzmann (MB) electron distributions can occur in small, transient laser-driven plasmas.

In this work, the long mean-free-path electrons are described by an MB distribution at a temperature  $T_h$  comprising a number fraction  $\epsilon$  of the total electron density. This “hot” component and the main population at the “cold” temperature  $T_c$  form a bi-Maxwellian distribution that is sufficiently general to study the most important effects of hot electrons on the bulk ionization state of plasmas and on their x-ray diagnostics. The most likely sources of hot populations in a cold background are suprathermal electrons from resonant absorption and high-energy electrons from an approaching heat front or from a hot, compressed target core. This report will not consider the source of hot electrons but will examine the sensitivity of x-ray emission to the presence of an assumed hot-electron population. The effect of a small, non-Maxwellian electron population on atomic process rates is considered in the interpretation of two kinds of experiments.

The first kind of experiment discussed is the burn-through, thermal transport experiment in which x-ray lines are emitted from highly ionized medium-Z atoms of a metal layer when a laser-driven heat front has penetrated an overcoated plastic layer of a given thickness. The “turn-on” of a particular spectral feature is interpreted in these experiments as a signal that a particular isotherm of the heat front has arrived at the metal layer. Hydrodynamic simulations of previous experiments<sup>1,2</sup> generally reproduced the observed penetration depths using thermal transport models consisting of the diffusive Spitzer-Härm transport model<sup>3</sup> with a maximum allowed thermal flux  $F_{\max}$  equal to a fraction  $f$  of the free-streaming electron energy flux

$$F_{\max} = f n_e k T_e (k T_e / m_e)^{1/2}, \quad (1)$$

where the “flux-limit parameter”<sup>4</sup>  $f$  lies within the range  $0.01 \leq f \leq 0.1$ . Recent experiments at LLE, however, have indicated penetration significantly deeper than can be calculated using the usual flux-limit formalism.<sup>5,6</sup> This report considers the extent to which this apparent deep penetration can be attributed to the turn-on of the signature line at a relatively low temperature well ahead of the heat front, where the

electron energy distribution is augmented by a small population of higher-energy electrons. Such a population could originate in the hot, laser-heated plasma and penetrate deep into the colder part of the plasma due to their relatively long mean free paths.

The second kind of experiment to be considered is the implosion of glass microballoons diagnosed in part by x-ray microscope images.<sup>7</sup> The time-integrated image of such an implosion seen in the 2- to 6-keV range is formed primarily by the recombination continuum from bare and H-like Si ions. The most prominent features in such images are an outer ring formed by the heat-front dwelling at its point of maximum excursion toward the center of the target and a central disc formed by emission from the inner surface of the glass shell as it is heated by the low-Z (DT) fill gas at maximum compression.

Numerically simulated images show considerable sensitivity to parameters such as the flux-limit parameter and the partition of laser energy into thermal and suprathermal electrons. By comparing these simulated images to the actual images, limits on these parameters can be set.<sup>7</sup> However, we find that the intensities of the inner feature are particularly sensitive to small ( $\leq 1\%$  by number) populations of hot (energy  $\geq$  few keV) electrons through their effect on atomic ionization and excitation rates; thus, the non-Maxwellian distribution can modify inferences made regarding the thermal flux inhibition and energy partitioning.

#### Line Turn-On in Non-Maxwellian Plasmas

To illustrate the effect of a small, hot-electron population on lowering the temperature for line emission, we calculate Lyman- $\alpha$  emission from an aluminum plasma, assuming collisional-radiative equilibrium with atomic ionization and transition rates modified for a non-Maxwellian electron spectrum. For the purposes of this report, a bi-Maxwellian distribution<sup>8</sup> of the form

$$f_{BM}(v, \epsilon, T_c, T_h) = (1 - \epsilon)f_{MB}(v, T_c) + \epsilon f_{MB}(v, T_h) \quad (2)$$

will suffice. This distribution is a linear combination of MB distributions evaluated at the hot  $T_h$  and background  $T_c$  temperatures, with  $\epsilon$  being the number fraction of electrons in the hot population. Collisional ionization, excitation and de-excitation, and radiative recombination rates for MB distributions are proportional to MB-weighted velocity integrals of their respective cross sections

$$R_{MB}(T) \propto \int \sigma(v) v f_{MB}(v, T) d^3v, \quad (3)$$

so that the bi-Maxwellian rates are also linear combinations of MB rates,

$$R(\epsilon, T_c, T_h) = (1 - \epsilon) R_{MB}(T_c) + \epsilon R_{MB}(T_h). \quad (4)$$

The most significant effect of the hot component on the ion populations is through the collisional ionization and excitation rates in which the most important temperature-dependent factor at the threshold of emission is the exponential term

$$R_{MB}(T) \sim \dots e^{-\chi/kT}, \quad (5)$$

where  $\chi$  is the relevant excitation or ionization energy. At  $T \sim 400$  eV, where the 1.7-keV Si Lyman- $\alpha$  line is seen, this exponential is of the order of  $10^{-2}$  for the needed excitation. For  $kT_h \geq \chi$ , this factor is nearly unity, so that a 1% hot population is as effective as the entire cold population in driving the ionization. Since the threshold exponential is near unity for any  $T_h$  value in excess of the threshold energy, the effect of the hot population will be relatively insensitive to the value of  $T_h$ .

The ions in the model used here are treated in the hydrogenic approximation.<sup>9</sup> Only singly excited states are considered, with the active electron orbiting in the field of a screened nucleus whose effective charge is calculated by subtracting the screening contribution of each core electron from the nuclear charge.<sup>10</sup> All ionization species are included in the population set. Excited states through principal quantum number  $n = 4$  are included in the hydrogen-, helium-, and lithium-like species. States are specified by principal quantum number only; the sublevels are assumed to be degenerate and equally populated. Continuum lowering of ionization energies is calculated according to the Stewart-Pyatt model.<sup>11</sup> Dielectronic recombination is not considered; it should have only a negligible effect on the ionic populations at the high densities ( $n_i \geq 10^{20} \text{ cm}^{-3}$ ) examined.<sup>12</sup>

The possible effect of the hot component of the electron energy distribution on the appearance of the Lyman- $\alpha$  line from the Al layer of a target can be determined from the steady-state solution to the population equations containing these rates. The results shown in Fig. 22.17 give the relative population of the Al Lyman- $\alpha$ -emitting state,

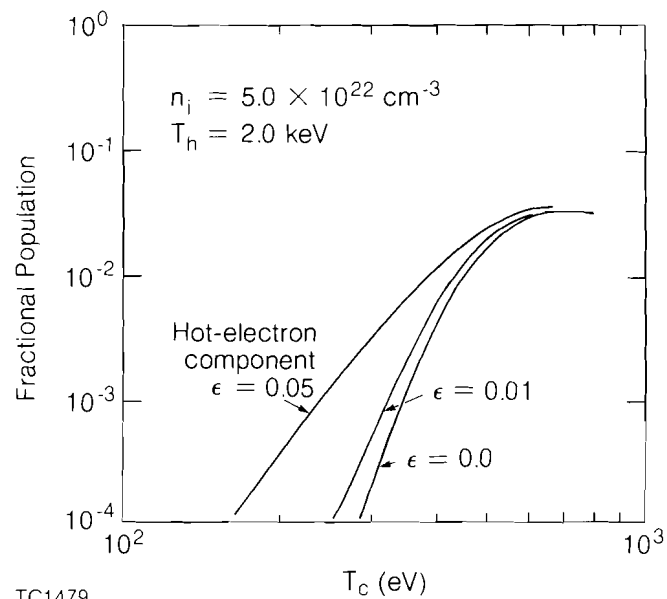


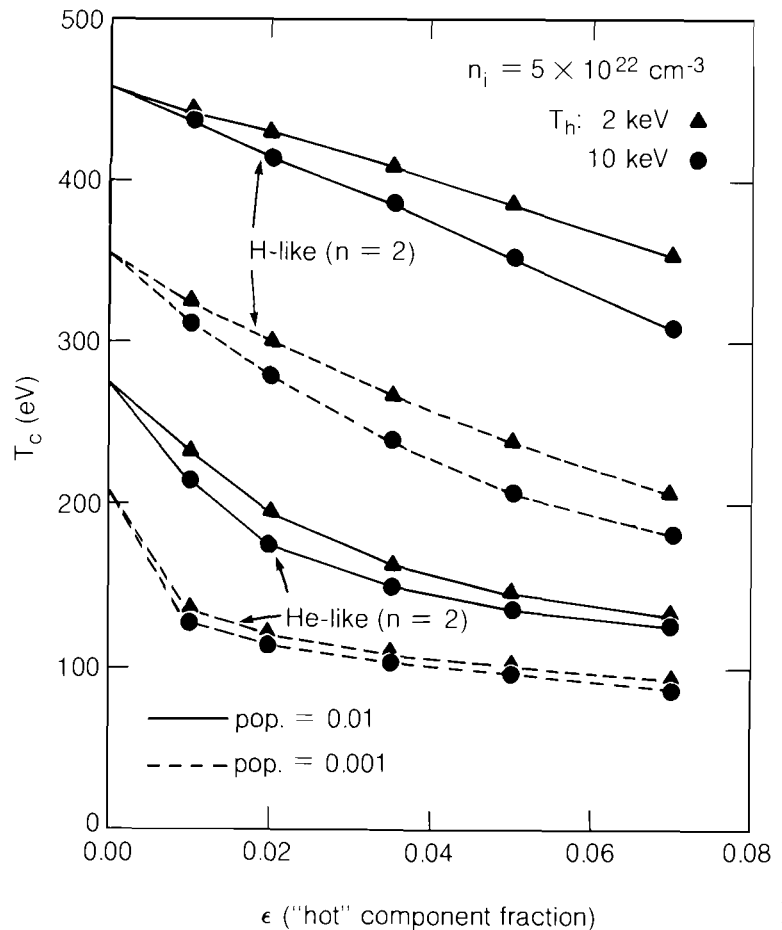
Fig. 22.17

The steady-state fractional population of the Lyman- $\alpha$ -emitting ( $n=2$ ) H-like species for optically thin conditions plotted as a function of  $T_c$  for various  $\epsilon$  values. The density assumed,  $n_i = 5.0 \times 10^{22} \text{ cm}^{-3}$ , is representative of conditions expected at the foot of the heat front. At marginal turn-on temperatures,  $T_c \sim 300\text{--}400$  eV, significant changes in the emitting population result from hot-electron fractions at  $\sim 1\%$  level.

Fig. 22.18  
 The background temperature  $T_c$  at which a fractional population of the Lyman- $\alpha$  (H-like,  $n=2$ )- or helium- $\alpha$  (He-like,  $n=2$ )-emitting species would reach values of 0.01 (—) or 0.001 (-----) is plotted as a function of the hot-electron population fraction  $\epsilon$ . The plasma conditions are the same as assumed in Fig. 22.17. The  $T_h = 2$ -keV ( $\blacktriangle$ ) and 10-keV ( $\bullet$ ) results are remarkably similar. Given a  $T_h$  value in this range of values well in excess of the relevant ionization energies, hot-electron populations at the 2–5% level can lower the background temperature value required to create these emitting-state populations of the order of 100 eV.

plotted as a function of the background temperature for an Al plasma at an ion density close to the solid density of  $6.0 \times 10^{22} \text{ cm}^{-3}$ , typical of what might be found ahead of the heat front. At a background temperature of 400 eV the population is near its peak value, and it drops rapidly at lower temperatures. The curves for additions of 1% and 5% 2-keV electrons show that these percentages of hot electrons do increase the emitting populations by significant factors. Thus, the background temperature at which a given population is reached can be reduced by adding a small hot-electron population.

The effect of the hot-electron population in lowering the background temperature at which a given emitting population exists is shown more clearly in Fig. 22.18. Curves representing the background temperature value at which either a 1% or 0.1% abundance of the H-like Lyman- $\alpha$ - or helium- $\alpha$ -emitting states occurs are plotted as functions of the hot-electron population fraction  $\epsilon$ . The results for hot-electron temperatures of 2 keV and 10 keV are remarkably similar. This confirms indirectly the conjecture made earlier that the results should be relatively insensitive

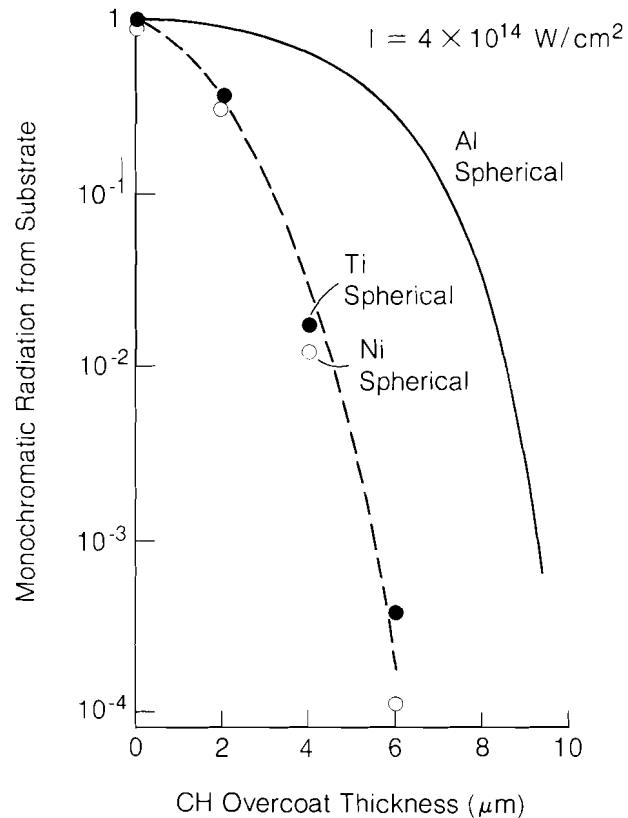


TC1481

to changes in  $kT_n$  well above threshold energies. It is seen that values of  $\epsilon$  of 2–5% are sufficient to reduce the  $T_c$  value for a given population by about 100 eV.

### Burn-Through Experiments

One experimental result that raises the possibility of non-Maxwellian effects on atomic transition rates is illustrated by the burn-through results shown in Fig. 22.19 for  $\lambda_L = 1054\text{-nm}$  illumination on various CH coating thicknesses over various substrate materials.<sup>5</sup> Similar results have been obtained recently with  $\lambda_L = 351\text{-nm}$  illumination.<sup>6</sup> The curves represent normalized intensities of specific emission lines. The CH thickness at which a given curve drops off by 10% can be taken as the penetration depth of a particular heat-front isotherm. The Al curves give the H-like Lyman- $\alpha$  intensity at 1.73 keV, which is expected to first appear at temperatures near 450 eV. The Ti and Ni curves representing their He-like  $2^1P\text{-}1^1S$  resonance lines at 4.75 keV and 7.8 keV, respectively, correspond similarly to the arrival of the  $\sim 1.0\text{-keV}$  and  $\sim 1.5\text{-keV}$  isotherms.



E3291

Fig. 22.19

Normalized curves showing the cutoff of the time-integrated line emission from various substrates with increasing CH overcoat thickness at constant-incident intensity of  $4 \times 10^{14} \text{ W/cm}^2$  under spherical illumination.<sup>5</sup> The aluminum curve shows the Lyman- $\alpha$  intensity that is expected to appear with the arrival of the 400-eV isotherm at the substrate. The intensities of the  $2^2P\text{-}1^1S$  resonance lines of He-like titanium and nickel signal temperatures of  $\sim 1.0 \text{ keV}$  and  $\sim 1.5 \text{ keV}$ , respectively.

The penetration of the 400-eV isotherm observed in the spherically illuminated Al experiments exceeds numerically simulated penetrations by roughly a factor of 3 for a broad range of flux-limit parameter values.<sup>5</sup> The penetration depths of the higher temperature isotherms

signaled by the Ti and Ni emission are much closer to predicted values. One straightforward interpretation of this result considered at the time this experimental result was reported is that flux-limited diffusion theory is inapplicable to this problem.<sup>5</sup> There might exist a low-temperature precursor or "foot" on the heat front that cannot be simulated without a nonlocal multigroup electron transport model. This foot is formed by the higher-energy, long mean-free-path electrons from behind the heat front penetrating into colder background material at a temperature  $T_c$ . A possible explanation of the premature turn-on of the Al emission is that the emission comes from substrate material at a background temperature much less than 400 eV, where the ionization and excitation of the aluminum is driven by the small hot-electron population. The likelihood of this explanation will be considered in terms of whether a plausible hot population can excite a sufficiently large population of emitting ions at values of  $T_c$  much less than the nominal 400-eV turn-on temperature.

The results discussed previously and illustrated in Fig. 22.19 tend to reinforce the earlier interpretations of the burn-through experiments based on Maxwellian atomic rates. A lowering of the Lyman- $\alpha$  turn-on temperature by 100 eV is probably not sufficient to account for the burn-through depths observed. Even a 1% hot-electron population, which would not lower the turn-on temperature sufficiently, would contain of the order of 10% of the plasma energy. Hot-electron populations of this size beyond the heating front are far larger than what appears to be plausible, based on available simulations of suprathreshold electron transport and multigroup Fokker-Planck simulations of thermal transport.<sup>13</sup> These results suggest that the magnitude of the non-Maxwellian effect is not large enough to explain the burn-through results and that other physical mechanisms must be sought.

### Images of Implosions

The x-ray image of an ablatively imploded DT-filled glass microballoon can be particularly sensitive to hot-electron populations when the temperature of the inner part of the glass shell is very close to the threshold for strong x-ray emission. The image of the emission is a potentially sensitive diagnostic of implosion dynamics and thermal transport because small changes in the inner part of the shell near this threshold can have a large effect on the image. The source of hot electrons in the shell inner region would be electrons of the "tail" of the distribution in the hot DT.

One such implosion image of 3-keV emission has previously been reported.<sup>7</sup> The image is formed primarily by the recombination continuum of the bare and H-like species of the silicon in the glass shell.

Theoretical simulations of the x-ray pinhole image of this implosion have been obtained by solving the equation of radiative transfer using the temperature and density history of the implosion calculated by the 1-D Lagrangian hydrocode *L/LAC*.<sup>14</sup> *L/LAC* includes separate ion and electron temperatures, flux-limited thermal electron transport, multigroup suprathreshold electron transport, ray tracing of the incident laser light, and multigroup radiation transport with tabulated LTE opacities.<sup>15</sup> Opacities and emissivities for the image simulation are calculated using

temperature and density information from the hydrocode solution, and atomic population information derived from the rate equations described earlier. The time-dependent atomic rate equations include K-shell photoionization and photoexcitation of the first two Lyman-series lines of the H-like and He-like species. Doppler line profiles are used at low densities, and Stark-broadened line profiles calculated by Hooper<sup>16</sup> are used at higher densities.

Figure 22.20 shows the shell conditions near peak compression of a simulation of this implosion, obtained using a flux-limit parameter  $f = 0.03$  and a suprathreshold-electron deposition fraction  $\eta_s = 0.16$ . The top plot shows the electron temperature and ion density of the shell, and the center plot shows the relative populations of the ground states of the bare, H-like, and He-like silicon species. The bottom plot illustrates the double-featured structure of the time-integrated image formed by the 3-keV emission from such an implosion. The intensity peaks in this image correspond with regions of relatively intense, recombination continuum emission in the plasma – at times near peak compression.

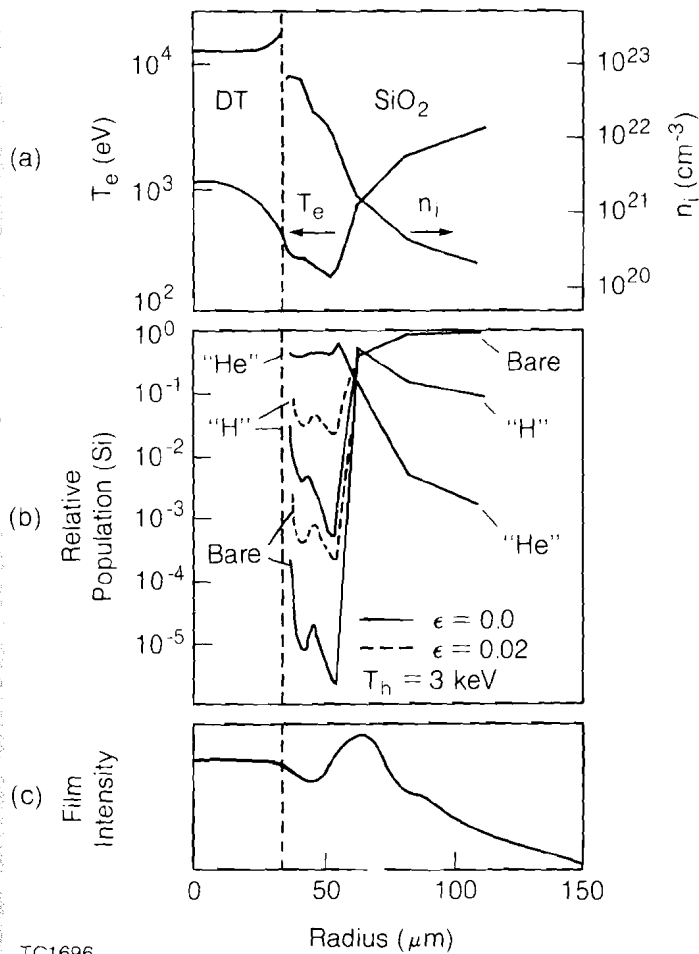


Fig. 22.20  
 Simulated peak-compression conditions in the imploded microballoon at a time near peak compression. The time-integrated recombination emission that forms the image shown in (c) as a radial trace is emitted primarily in the  $\sim 200$ -ps time interval when these peak conditions prevail. The temperature and density are plotted in (a), and the population fractions of the ground states of the three most highly ionized silicon species are plotted in (b). The dashed lines in (b) show how the primary emitting populations are raised by the presence of the 2% hot-electron population.

The higher emissivity results from high abundances of the H-like and bare species, from the high temperatures near the ablation front, and from the high temperature and density near the glass-DT interface.

Figure 22.21 shows several image simulations for this implosion. Similar image simulations were prepared from hydrocode results using other values of  $f$  and  $\eta_s$ . The solid curve in Fig. 22.21 is the non-LTE result based on Maxwellian atomic rates, and the dashed curve was obtained using LTE atomic populations. The limits  $\eta_s < 0.20$  and  $0.03 \leq f < 0.08$  have been inferred for this implosion based upon the resemblance of simulated LTE images to the densitometer trace, particularly in the occurrence of distinct inner and outer features that are comparable in intensity.<sup>7</sup> The images shown in Fig. 22.21 were obtained assuming specifically  $f = 0.03$ . The close resemblance in shape between the LTE and non-LTE images in Fig. 22.21 was also obtained for other simulations based on plausible values of  $f$  and  $\eta_s$ . In non-LTE, nonstatistical balances of inverse processes and finite ionization rates tend to reduce the degree of ionization from that obtained in LTE. This accounts for the non-LTE image being less intense overall than the LTE image, but not for the similarity in structure between these two images. This similarity is probably fortuitous, but it nevertheless supports inferences drawn from comparisons of the observed image with the results of LTE image simulations.<sup>5</sup>

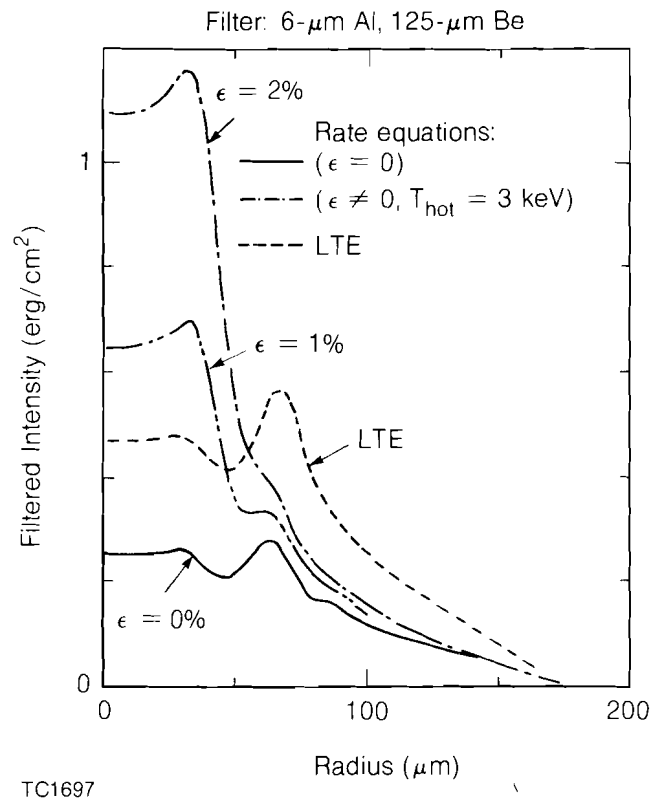


Fig. 22.21  
Radial traces of the simulated pinhole image intensity from the microballoon implosion for various assumptions, including LTE atomic populations and various hot-electron fractions and energies. The hot electrons affect the inner feature most strongly since the background temperature there is relatively cool.

The two remaining image curves in Fig. 22.21 were obtained assuming various hot-electron populations. For convenience, the values of  $\epsilon$  and  $T_h$  were assumed to be constant throughout the glass shell, but they only have a significant effect in the emitting region of interest. Since the shell material emitting the outer-feature radiation is already at  $T_e \sim 1$  keV, the additional hot population has a negligible effect on this feature. The inner feature, however, is formed by emission from a 300-eV environment in which the small hot-electron populations affect the emitting populations markedly, as can be seen from the dashed curves in Fig. 22.20(b). This results in a significantly enhanced inner feature. The images obtained for value of  $T_h = 3$  keV resemble the curves obtained for any value of  $T_h$  close to or above this value because of the threshold effect previously discussed.

The hydrocode simulation upon which the images in Fig. 22.21 are based used a flux-limit parameter of  $f = 0.03$ . The observed equal intensities of the inner and outer features correspond to a case intermediate between the  $\epsilon = 0.0$  and  $\epsilon = 0.01$ ;  $T_h = 3$ -keV curves shown at roughly  $\epsilon \approx 0.001$ . A similar set of curves based on simulations using  $f = 0.05$  gives a reasonably close resemblance to the observed image with  $\epsilon = 0.0$ . Assuming  $f=0.08$  gives a much too intense inner feature, one could then take  $f=0.05$  as a rough "best estimate," given the simplest hypothesis  $\epsilon=0.0$ . If it is only assumed that  $\epsilon$  is non-negative, then  $f = 0.05$  becomes an upper limit rather than an estimate. Significantly lower values of  $f$  cannot be ruled out without adequate upper limits on  $\epsilon$  at  $10^{-3}$  level.

It should be pointed out that changes in the shape of x-ray spectral lines can be expected from added hot electrons. The Si helium- $\beta$  profile in Fig. 22.22 is a superposition of emission from the low-density corona and from the high-density compressed core. As seen in the simulated line profiles, the helium- $\beta$  line acquires a Stark-broadened component from emission at high density as the hot electrons in the dense inner shell excite the relatively abundant He-like ground population (see Fig. 22.20). The few-percent hot-electron populations required in the inner shell in this example are not likely to occur, but if the inner temperature were higher, then a smaller fraction of hot electrons would be required to produce observable effects in the wings of the line.

### Conclusion

This report serves in part as a preliminary assessment of the importance of non-Maxwellian electrons in interpreting x-ray diagnostics of laser-fusion experiments. If hot populations of more than at least a few percent are ever shown to be plausible, then hot-electron effects on line spectra from burn-through experiments will be an important consideration. The shape of x-ray images appears to be much more sensitive to hot electrons, perhaps sufficiently so to warrant a more detailed treatment of thermal electron transport in the simulation of images. These results are probably more significant as an assessment of the sensitivity of these diagnostics to given levels of hot-electron abundance, rather than as an assessment of the absolute importance of hot-electron effects. In view of the tentative state of thermal transport theory as applied to full simulations of these experiments, any speculation about the plausibility of a given hot-electron population level should also be regarded as tentative.

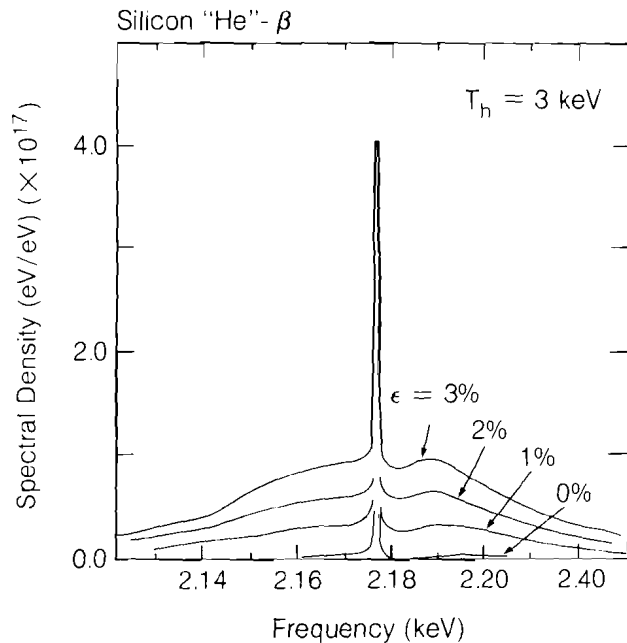


Fig. 22.22

Simulated time-integrated spectral intensity plotted near the Si helium-like  $\beta$  line. As the fractional population of  $T_h = 3\text{-keV}$  electrons is increased, Stark-broadened emission from the dense inner shell increases.

#### ACKNOWLEDGMENT

This work was supported by the U.S. Department of Energy Office of Inertial Fusion under agreement number DE-FC08-85DP40200 and by the Laser Fusion Feasibility Project at the Laboratory for Laser Energetics which has the following sponsors: Empire State Electric Energy Research Corporation, General Electric Company, New York State Energy Research and Development Authority, Northeast Utilities Service Company, Ontario Hydro, Southern California Edison Company, The Standard Oil Company, and University of Rochester. Such support does not imply endorsement of the content by any of the above parties.

#### REFERENCES

1. B. Yaakobi, T. Boehly, P. Bourke, Y. Conturi, R. S. Craxton, J. Delettrez, J. M. Forsyth, R. D. Frankel, L. M. Goldman, R. L. McCrory, M. C. Richardson, W. Seka, D. Shvarts, and J. M. Soures, *Opt. Commun.* **39**, 175 (1981).
2. W. C. Mead *et al.*, *Phys. Fluids* **27**, 1301 (1984); A. Hauer *et al.*, *Phys. Rev. Lett.* **53**, 2563 (1984).
3. L. Spitzer and R. Härm, *Phys. Rev.* **89**, 977 (1953).
4. R. C. Malone, R. L. McCrory, and R. L. Morse, *Phys. Rev. Lett.* **34**, 721 (1975).
5. B. Yaakobi, J. Delettrez, L. M. Goldman, R. L. McCrory, R. Marjoribanks, M. C. Richardson, D. Shvarts, S. Skupsky, J. M. Soures, C. Verdon, D. M. Villeneuve, T. Boehly, R. Hutchison, and S. Letzring, *Phys. Fluids* **27**, 516 (1984).

6. LLE Review **17**, 32 (1983); B. Yaakobi, O. Barnouin, J. Delettrez, L. M. Goldman, R. Marjoribanks, R. L. McCrory, M. C. Richardson, and J. M. Soures, *J. Appl. Phys.* (to be published).
7. J. Delettrez, presented at the 14th Annual Anomalous Absorption Conference, Charlottesville, VA, 1984, paper G11; LLE Review **20**, 160 (1984).
8. R. Epstein, S. Skupsky, J. Delettrez, and B. Yaakobi, *Bull. Am. Phys. Soc.* **28**, 1219 (1983); J. P. Apruseze and J. Davis, *Phys. Rev. A* **28**, 3686 (1983).
9. H. Mayer, Los Alamos Report No. AECD-1870 (1947), quoted in G. C. Pomraning, *The Equations of Radiation Hydrodynamics* (Pergamon Press, New York, 1983), pp. 168-169.
10. J. C. Slater, *Phys. Rev.* **36**, 57 (1930), quoted in G. C. Pomraning, *op. cit.*
11. J. C. Stewart and K. D. Pyatt, *Astrophys. J.* **144**, 1203 (1966).
12. D. Salzmann and A. Krumbein, *J. Appl. Phys.* **49**, 3229 (1978).
13. J. Delettrez (unpublished).
14. Earlier versions of *LILAC* are described in LLE Reports No. 16 (1973) and No. 36 (1976).
15. W. F. Huebner, A. L. Merts, N. H. Magee, and M. F. Argo, Report No. LA-6760, 1977 (unpublished).
16. R. J. Tighe and C. F. Hooper, *Phys. Rev. A* **17**, 410 (1978); C. F. Hooper (private communication).

## Section 3

# ADVANCED TECHNOLOGY DEVELOPMENTS

### 3.A Synchronously Pumped, Colliding-Pulse, Mode-Locked Dye Laser

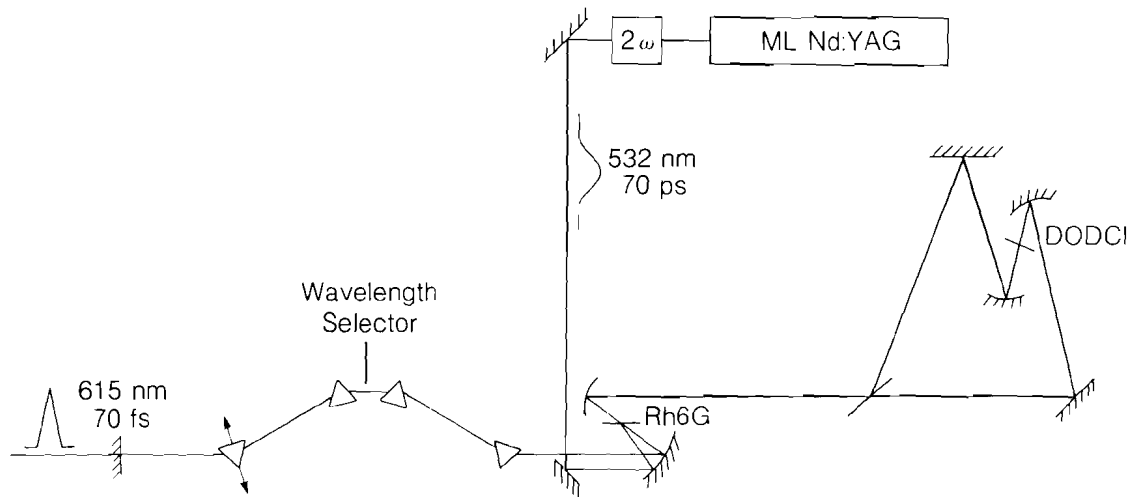
Remarkable advances in the development of ultrashort pulse dye lasers and amplifiers have been made in the past few years, permitting the study of ultrafast nonlinear phenomena on the subpicosecond time scale. In particular, the development of colliding-pulse mode-locking (CPM),<sup>1</sup> combined with direct control of the dye oscillator dispersion and phase modulation properties, has enabled the generation of stable optical pulses shorter than 100 fs.

Normally, the CPM laser is cw-pumped by an Argon-ion laser, and the pulses are amplified with pump pulses of duration of the order of 10 ns, usually from a Q-switched Nd:YAG laser or a copper vapor laser. There are advantages to be gained, however, by synchronous amplification with pump pulses shorter than 100 ps.<sup>2,3</sup> These advantages include increased efficiency, stability, and energy contrast between the amplified pulse and amplified spontaneous emission (ASE). Amplification with short pump pulses requires a strict ( $\sim 20$ -ps) synchronization between the pump and oscillator pulses. This requirement necessitates that the dye oscillator be synchronously pumped. We report here the development of a dye laser that combines the advantages of synchronous pumping, colliding-pulse mode-locking, and tunable intracavity group velocity dispersion (GVD).

A necessary condition for the dye laser to be both synchronously pumped and colliding-pulse mode-locked is that the critical position of the saturable absorber be unaffected by adjustments of the cavity

length. The use of an antiresonant ring as one end mirror of a linear cavity<sup>4</sup> enables this condition to be satisfied. An antiresonant ring consists of a 50% splitter and two mirrors to return the beams to the splitter. An incoming pulse from the linear part of the cavity is split into two equal parts by the 50% splitter; when the two pulses recombine on the splitter, they interfere so that the entire pulse is returned to the cavity. As suggested by Siegman<sup>5</sup> and subsequently demonstrated with Q-switched Nd:YAG<sup>6</sup> and Nd:glass<sup>7</sup> lasers, colliding-pulse mode-locking may be achieved by placing a saturable absorber exactly halfway around the antiresonant ring from the 50% splitter.

A diagram of the dye laser is shown in Fig. 22.23. The laser consists of a four-mirror linear cavity, where one end mirror is a 5%-output coupler mounted on a translation stage, and the other is an antiresonant ring. The gain medium is a 200- $\mu\text{m}$  jet of Rhodamine 6G in ethylene glycol, and the saturable absorber is a 20- $\mu\text{m}$  jet of 3,3'-diethyloxadicarbo-cyanine iodide (DODCI) in ethylene glycol.



E3292

Fig. 22.23 Synchronously pumped, colliding-pulse, mode-locked dye laser. The laser consists essentially of a four-mirror linear cavity, where the antiresonant ring acts as one end mirror. Four Brewster prisms are included to control the intracavity dispersion.

The dye laser is synchronously pumped at 100 MHz by the frequency-doubled output of a cw mode-locked Nd:YAG laser; the pump power is typically 1.5 W, and the pump pulse width is about 70 ps. Both the Nd:YAG pump laser and the dye laser are mounted on super Invar slabs to minimize cavity length fluctuations. The shortest pulses and greatest stability are obtained when the cavity lengths are properly matched and the Nd:YAG laser cavity length is adjusted to minimize the phase jitter of the Nd:YAG output. In this case, the dye laser stability is comparable to that of the pump, which is approximately 1% rms for frequency-doubled Nd:YAG.

The four Brewster prisms are placed in the linear part of the cavity to control the cavity GVD. As first demonstrated by Fork *et al.*,<sup>8</sup> the

angular dispersion of the prisms causes negative GVD. The dispersion of the prism glass, however, is positive (normal). By translating one of the prisms normal to its base, as shown by the arrows in Fig. 22.23, the amount of glass in the cavity — i.e., the amount of positive GVD — may be continuously adjusted without changing the negative GVD. In this way it is possible to tune the cavity GVD through zero. This is important, because the GVD, due to dielectric mirror coatings and the gain and absorber media, becomes extremely critical for pulses shorter than about 200 fs. Furthermore, theoretical studies of ultrashort pulse lasers have shown that soliton-like pulse shaping, where positive self-phase modulation (SPM) is balanced by negative GVD, can occur in an ultrashort pulse laser, yielding shorter and more stable pulses than are otherwise obtainable.<sup>9</sup>

With a DODCI concentration of about  $2 \times 10^{-3}$  M, the dye laser output is 60 mW at 616 nm. Pulse widths as short as 70 fs can be obtained; a pulse autocorrelation is shown in Fig. 22.24. The usefulness of the Brewster prism arrangement is apparent since the minimum pulse width we have attained without the prisms is 85 fs, and the long-term stability of the laser is greatly improved.

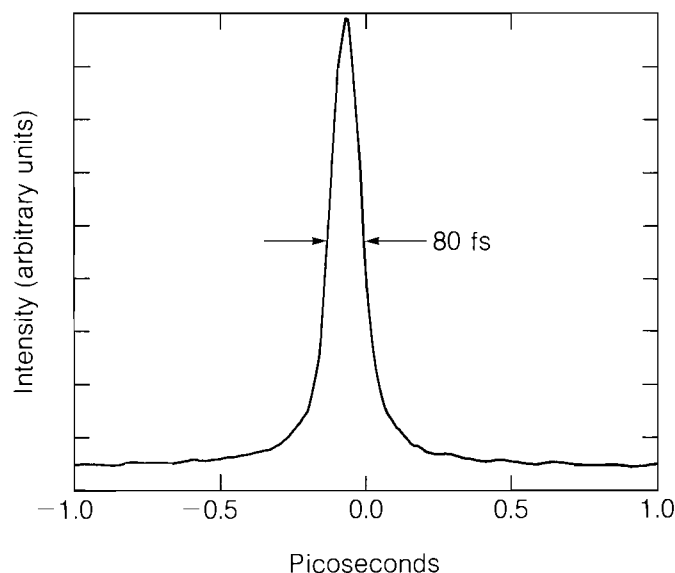


Fig. 22.24  
Autocorrelation of the dye laser output. The correlation width is 106 fs, corresponding to a real pulse width of 70 fs, assuming a  $\text{sech}^2$  pulse shape.

E3549

The dependence of the laser pulse width on the net cavity GVD (i.e., on the amount of intracavity glass relative to the zero-GVD point) is displayed in Fig. 22.25. Note that not only is there a sharp minimum in the pulse width, but also the pulse shape and spectrum differ qualitatively in two different regions of the graph. When there is too little glass in the cavity, the pulse has negligible wings, the spectrum tails to the yellow, and the time-bandwidth product  $\tau_p \Delta\nu$  is about 0.35. When there is too much glass in the cavity, the pulse has broad wings, the spectrum tails to the red, and  $\tau_p \Delta\nu$  is about 0.5. Near the minimum of

the curve in Fig. 22.25, the spectrum is symmetric. The minimum pulse width occurs with approximately 50 to 100  $\mu\text{m}$  less glass in the cavity than with the prism position, which yields a symmetric spectrum. This is consistent with the picture of soliton-like pulse shaping mentioned above.

Future improvements to the laser will include the use of dielectric mirror coatings with controlled dispersion properties, and control of the intracavity SPM (principally through more careful control of the gain and absorber saturation characteristics).

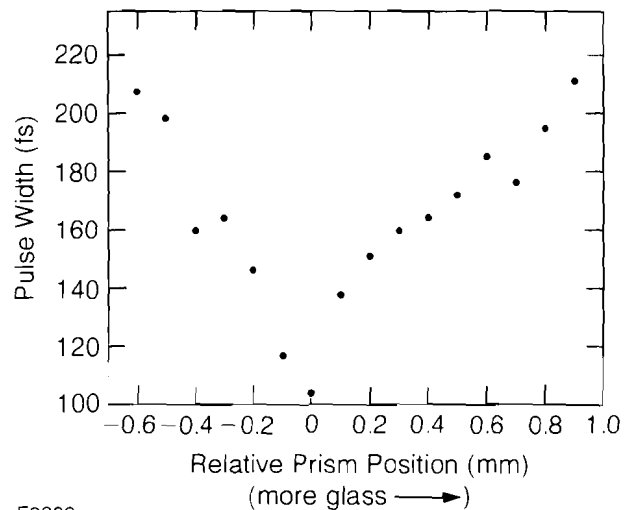


Fig. 22.25  
Pulse width versus relative prism position. The pulse width decreases to a sharp minimum and then increases as the amount of glass in the cavity is increased.

In conclusion, we have developed a synchronously pumped, colliding-pulse mode-locked dye laser that produces pulses of duration down to 70 fs suitable for synchronous amplification. The system is based on a cw mode-locked Nd:YAG laser, so that kilohertz-repetition-rate synchronous amplification is possible using a recently developed regenerative Nd:YAG amplifier.<sup>10</sup> This oscillator-amplifier system produces ultrashort, microjoule pulses at a high repetition rate suitable for white-light continuum generation and subpicosecond time-resolved spectroscopy.

#### ACKNOWLEDGMENT

This work was supported by the following sponsors of the Laser Fusion Feasibility Project at the Laboratory for Laser Energetics—Empire State Electric Energy Research Corporation, General Electric Company, New York State Energy Research and Development Authority, Northeast Utilities Service Company, Ontario Hydro, Southern California Edison Company, The Standard Oil Company, and University of Rochester. Such support does not imply endorsement of the content by any of the above parties.

#### REFERENCES

1. R. L. Fork, B. I. Greene, and C. V. Shank, *Appl. Phys. Lett.* **38**, 671 (1981).
2. T. Sizer II, J. D. Kafka, A. Krisiloff, and G. Mourou, *Opt. Commun.* **39**, 259 (1981).

3. T. Sizer II, J. D. Kafka, I. N. Duling III, C. W. Gabel, and G. A. Mourou, *IEEE J. Quant. Electron.* **QE-19**, 506 (1983).
4. A. E. Siegman, *IEEE J. Quant. Electron.* **QE-9**, 247 (1973).
5. A. E. Siegman, *Opt. Lett.* **6**, 334 (1981).
6. H. Vanherzeele, J. L. VanEck, and A. E. Siegman, *Appl. Opt.* **20**, 3484 (1981).
7. J. M. Buchert, D. K. Basa, C. Tzu, and R. R. Alfano, *J. Appl. Phys.* **55**, 683 (1984).
8. R. L. Fork, O. E. Martinez, and J. P. Gordon, *Opt. Lett.* **9**, 150 (1984).
9. O. E. Martinez, J. P. Gordon, and R. L. Fork, in *Ultrafast Phenomena IV*, edited by D. H. Auston and K. B. Eisenthal, (Springer, New York, 1984).
10. I. N. Duling III, T. Norris, T. Sizer II, P. Bado, and G.A. Mourou, *J. Opt. Soc. Am. B* **2**, 616 (1985).

### 3.B Dynamically Loaded Scratch Tester for Thin-Film Adhesion Measurements

The American Society for Testing and Materials (ASTM) defines adhesion as the state in which two surfaces are held together by interfacial forces, which may consist of valence forces or mechanical forces or both.<sup>1</sup> Mittal<sup>2</sup> describes the sum of all interfacial intermolecular reactions as "basic adhesion." He uses the term "practical adhesion" to represent the forces needed to disrupt the adherate-adherend system, either at the interface of the two, or in the interfacial region. The interfacial region (interphase) can be either a contamination layer on the substrate (oxides, oils, etc.) or it can be formed by the diffusion of the adhering materials.

The "practical adhesion" of dielectric thin-film antireflecting (AR) and highly reflecting (HR) coatings to optical glass and crystalline substrates is of considerable importance to LLE. Optics in OMEGA are periodically cleaned with a methanol-tissue wipe to remove dust. This type of routine maintenance can be performed on hard, well adhered coatings with no deleterious effects. More important, the laser-damage resistance of well adhered, hard dielectric films is thought to be superior to that of more weakly adhered films,<sup>3</sup> although experiments performed to demonstrate this correlation have not been conclusive.<sup>4,5</sup>

Because of our long-term interest in laser-damage-resistant coatings (refer to previous articles in LLE Review **7**, p. 2; **14**, p. 36; **20**, p. 175), we have sought to develop a reliable diagnostic for measuring relative adhesive strength in our thin-film coating facility. The standard, military cellophane-tape pull test,<sup>6</sup> and tests such as the plug pull test, topple

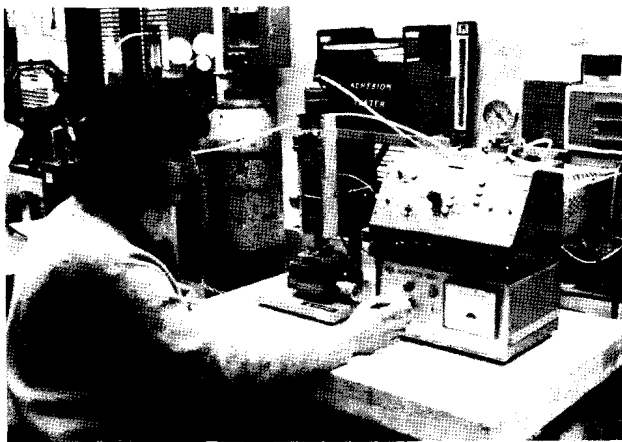
test, and peel test,<sup>7</sup> yield only vague, qualitative pass/fail data, or simply do not work for hard dielectrics deposited with modern techniques.

At LLE we have improved the scratch test, originally developed by Heavens<sup>8</sup> and theoretically enhanced by Benjamin and Weaver.<sup>9</sup> Our objective is to develop a rapid and reliable method for measuring the relative adhesive strength of samples within a given coating-substrate system as a function of any of the following parameters: substrate surface polishing, substrate cleaning, coating deposition method, substrate temperature during deposition, and post-deposition baking.

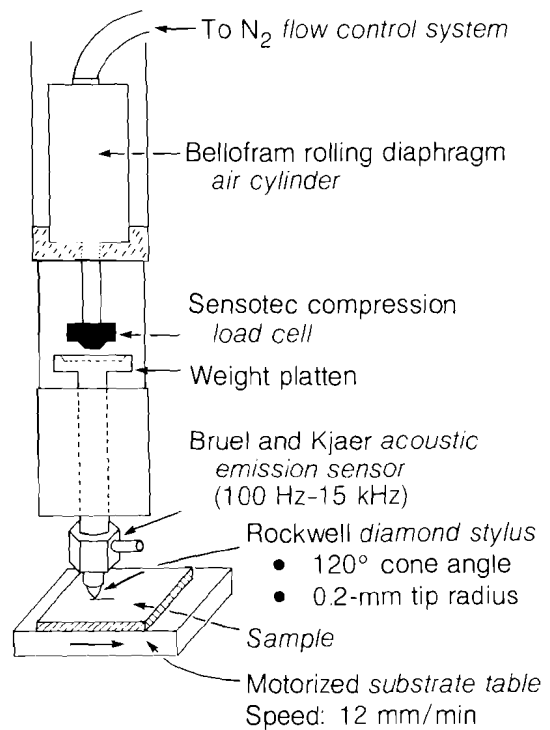
Our approach, which we refer to as dynamically loaded scratch testing,<sup>10</sup> minimizes the damaged regions of a coated part, yields real-time information in certain circumstances, and provides for the possibility of a limited amount of spatially resolved information. Specifically, by making in-house modifications to a commercial unit, we have developed a scratch tester that continuously increases the load applied using a spherical diamond stylus to a coated part in motion. The critical load for coating delamination is detected with an acoustic emission sensor (real-time) adjacent to the stylus, or with Nomarski microscopy. Adhesion information can be obtained with one scratch with a linear extent less than 2 mm. In this initial work we have addressed two problems:

Fig. 22.26

Dynamically loaded scratch tester with acoustic emission. Our modifications to the commercial unit include the addition of a flowing gas load system and load sensor. The modified apparatus linearly increases load during the scratching process.



BASIC UNIT: Manual revetest with acoustic emission  
Laboratoire Suisse de Recherches Hologères



G1388

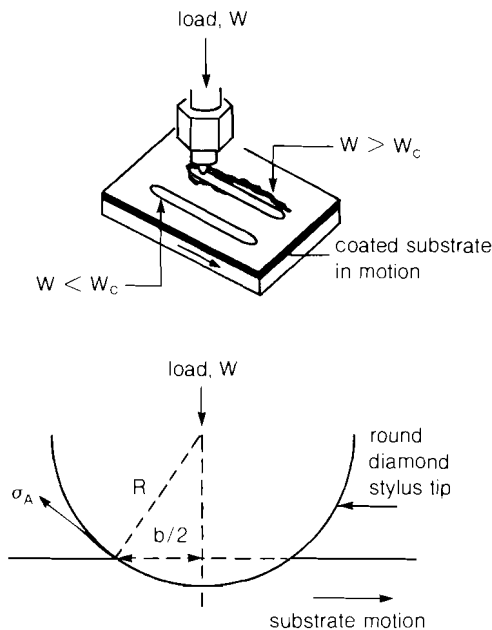
- (1) How useful is the acoustic emission feature as a sensor of adhesive failure for optical coatings?
- (2) Which optical coating-substrate systems exhibit adhesive failure within the loading range of the tester?

The dynamically loaded scratch tester is shown in the photograph at the left-hand side of Fig. 22.26. Details of the apparatus are given in the schematic diagram on the right-hand side of Fig. 22.26. Major modifications to the commercial unit<sup>11</sup> include the compression-loading capability consisting of an N<sub>2</sub> gas flow and control system, rolling diaphragm air cylinder, and compression load cell. With this apparatus and a dual pen chart recorder we can monitor the acoustic emission signal (y-axis) as a function of increasing load (x-axis).

In principle, at low loads  $W$ , deformation to the coating surface may occur with no adhesive failure. In Fig. 22.27 we illustrate how, when the applied load reaches some critical value  $W_c$ , the coating peels away from the substrate. It is the acoustic emission accompanying the coating-substrate separation process that we attempt to measure.

The equation accompanying Fig. 22.27 gives an expression for the actual adhesion strength of the coating, and the strength is proportional to the hardness  $H$  of the substrate divided by the stylus-tip radius  $R$ . It can alternately be expressed in terms of the indented track width  $b$  if

Fig. 22.27  
Critical load and adhesion strength. The critical load  $W_c$  for coating removal can be related to the adhesion strength of the thin film with knowledge of substrate hardness and, under certain conditions, of plastic deformation.



$$\sigma_A \cong \frac{1}{\pi^{1/2} R} (W_c H)^{1/2} \text{ or } \frac{2 W_c}{\pi R b}$$

WHERE . . .

- $\sigma_A$  = adhesion strength (kgf/mm<sup>2</sup>)
- $R$  = radius of stylus point (mm)
- $W_c$  = detected critical load (kgf)
- $b$  = width of track caused by  $W_c$  (mm)
- $H$  = hardness of substrate (kgf/mm<sup>2</sup>)

ASSUMING . . .

- $R \gg b$
- Substrate deformation is plastic.

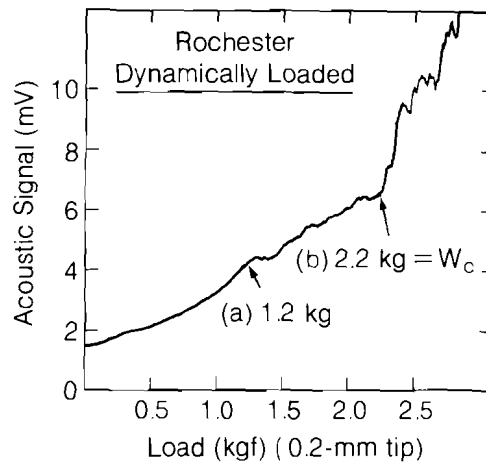
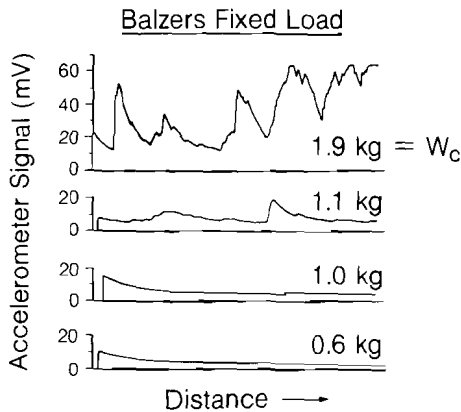
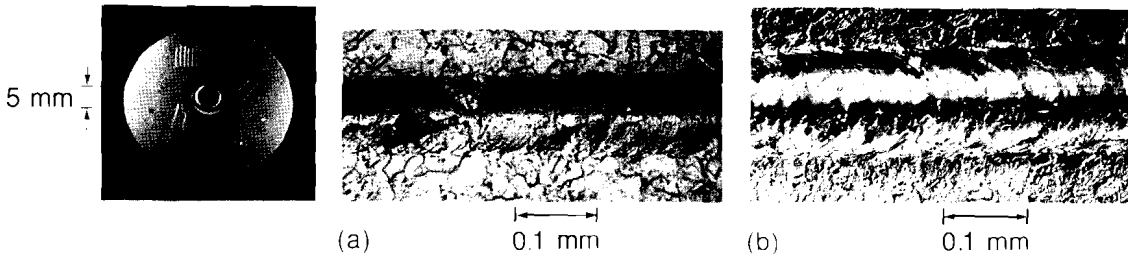
\*From ref. 9

hardness is unknown, provided that  $b \ll R$ . Several articles in the literature<sup>12,13</sup> dispute the validity of Benjamin and Weaver's interpretation of the scratch test when it is used to compare different hard-coating-substrate systems. For our present work we seek values of critical load only within a given system and not among different systems.

We performed an initial experiment in conjunction with A. J. Perry (Balzers, AG) to verify the accuracy of our modified apparatus. He and others have used the standard commercial unit to evaluate nonoptical coating-substrate systems with considerable success.<sup>13,14</sup> Figure 22.28 shows his results (left side) versus ours (right side) for chemical-vapor-deposited (CVD) TiN on stainless steel, on samples he provided. The increasing fixed load and dynamically loaded results give the same value of critical load within 7%. The utility of acoustic emission sensing is also apparent for this nonoptical coating system. In fact, using acoustic emission, it is possible to locate regions of the coating that fail at loads significantly below  $W_c$  (refer to region a) in both the plot and the micrograph of Fig. 22.26 at a load of  $W = 1.2$  kg. Perry interprets this as conclusive evidence for localized regions of poor adhesion.<sup>13</sup>

Fig. 22.28 Comparison of conventional and dynamically loaded scratch tests for CVD TiN on stainless steel. Measured critical loads are in excellent agreement using acoustic emission sensing for this nonoptical system. The advantage of using the dynamically loaded apparatus lies in the operator's ability to obtain  $W_c$  from a single scratch.

Coating thickness: 8.5  $\mu\text{m}$



\*Test samples and data provided by A. J. Perry (Balzers, AG)

G1494

Our attempts to extend the utility of dynamically loaded scratch testing to systems with optical applications are summarized in Table 22.1. We have examined glass, single crystal and polycrystalline substrates, and many different coating materials using three deposition methods. Results have been mixed. In several instances we have detected substrate fracture prior to coating removal, as determined after careful examination with Nomarski microscopy. This observation is noted in Table 22.1 and illustrated in Fig. 22.29 for CdS on borosilicate (BSC) glass. The acoustic signal in this case is derived from the fracture of the glass surface at loads near 2.7 kg, and not from the removal of the coating which occurs above 3.5 kg.

| Substrate*                          | Coating                        | (Method)        | Physical Thickness (μm) | Observations w/ 0.2-mm Tip                                 |
|-------------------------------------|--------------------------------|-----------------|-------------------------|--|
| • Stainless Steel                   | TiN                            | (CVD)           | 8.5                     | useful results w/ acoustic signal                          |
| • Irtran II<br>ZnS (PC)             | Ta <sub>2</sub> O <sub>5</sub> | (E-gun)         | 1.0                     | useful results w/o acoustic signal                         |
| • BSC Glass                         | CdS                            | (E-gun)         | 0.08                    | substrate fracture before coating removal                  |
|                                     | HfO <sub>2</sub>               | (E-gun)         | 1.0                     | useful results w/o acoustic signal                         |
| • Irtran I<br>MgF <sub>2</sub> (PC) | Nd <sub>2</sub> O <sub>3</sub> | (thermal)       | 0.3                     | substrate fracture . . . . .                               |
|                                     | SiO <sub>2</sub>               | (etch, sputter) | 0.75                    | substrate fracture . . . . .                               |
|                                     | Ta <sub>2</sub> O <sub>5</sub> | (E-gun)         | 1.0                     | useful results w/o acoustic signal                         |
|                                     | ZnS/ThF                        | (thermal)       | multilayer stack        | useful results w/o acoustic signal                         |
| • Fused Silica                      | Ta <sub>2</sub> O <sub>5</sub> | (E-gun)         | 10.0                    | substrate fracture before coating removal                  |
| • Ge (SC)                           | Al <sub>2</sub> O <sub>3</sub> | (E-gun)         | 1.0                     | useful results w/o acoustic signal                         |
| • Si (SC)                           | SiO                            | (thermal)       | 0.37                    | useful results w/o acoustic signal;<br>cleaning experiment |
|                                     | Nd <sub>2</sub> O <sub>3</sub> | (thermal)       | 0.3                     | substrate fracture . . . . .                               |
|                                     | SiO <sub>2</sub>               | (sputtered)     | 0.75                    | useful results w/ acoustic signal;<br>cleaning experiment  |
|                                     | TiO <sub>2</sub>               | (E-gun)         | 0.75                    | useful results w/o acoustic signal                         |
|                                     | Ta <sub>2</sub> O <sub>5</sub> | (E-gun)         | 1.0                     | useful results w/o acoustic signal;<br>cleaning experiment |
|                                     | Al <sub>2</sub> O <sub>3</sub> | (E-gun)         | 1.0                     | useful results w/o acoustic signal;<br>cleaning experiment |

\* PC = polycrystalline, SC = single crystal

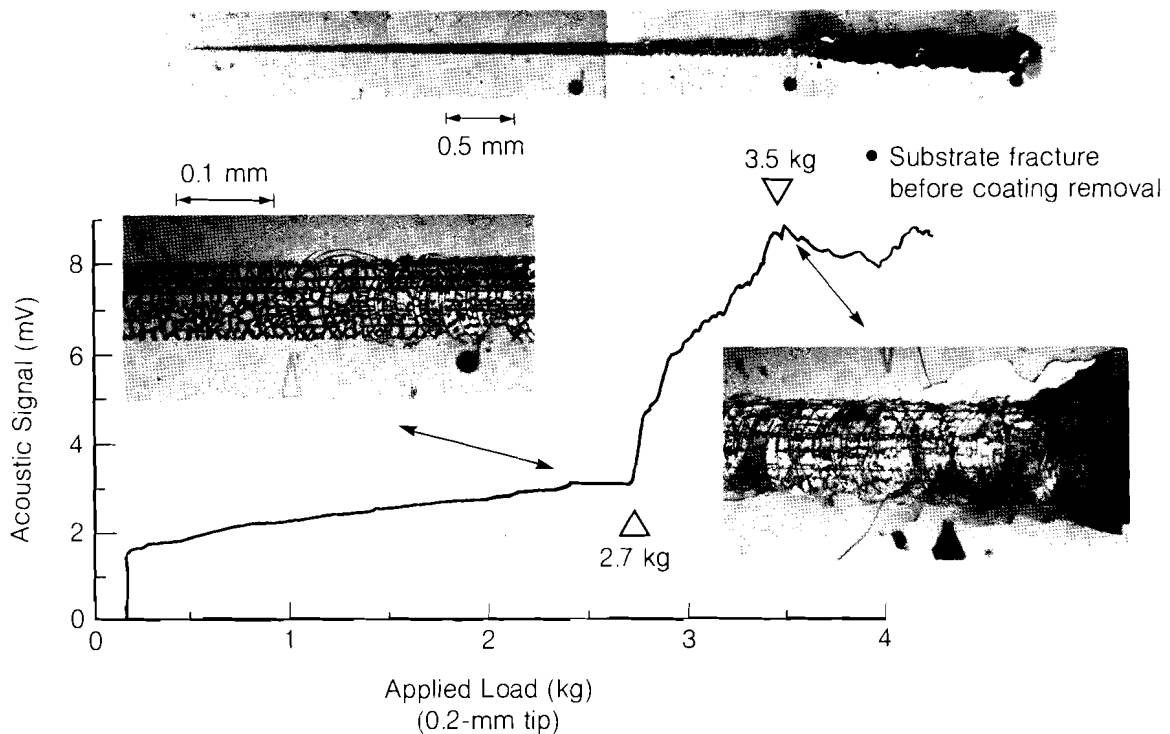
G1495, G1496

Table 22. 1  
Extension of adhesion measurements to systems with optical applications.

Other systems we sampled have given useful results when examined with Nomarski microscopy, but usually without any real-time acoustic signal. Three substrate cleaning experiments will be reviewed here.

**Substrate Cleaning Experiment 1**

We examined the effect of three standard cleaning processes upon the adhesion of metal oxides to the (111) surface of electronic-grade



G1410

Fig. 22.29

Results for 800-Å-thick CdS film on borosilicate (BSC) glass. The substrate fractured at a load of 2.7 kg prior to the occurrence of coating removal at 3.5 kg. The acoustic emission corresponds to the initiation of substrate fracture. This sequence of events invalidates the test for coating adhesion.

silicon. Twelve samples 25 mm × 25 mm × 1.5-mm thick were cut from three wafers. Cleaning was performed using one of the following:

- HPLC alcohol wipe
- Aqueous/Ultrasonic/UV(185 nm)-Ozone<sup>15</sup>
- Liquinox/DI water/Freon T-DFC

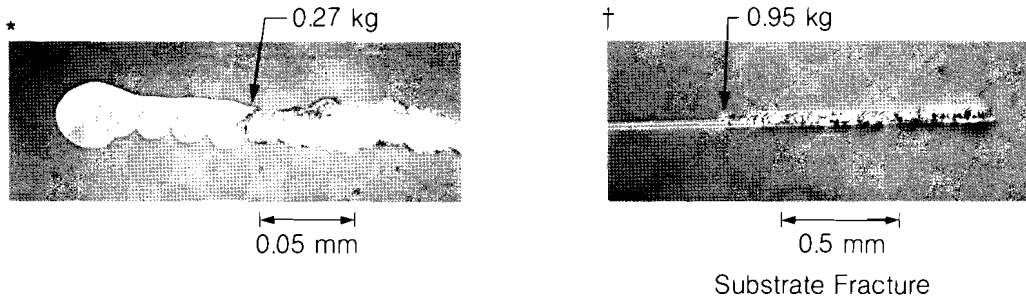
SiO was deposited using resistance evaporation at  $2 \times 10^{-5}$  Torr to a physical thickness of  $0.37 \mu\text{m}$  on parts cleaned in each of the above ways. Ta<sub>2</sub>O<sub>5</sub> was deposited using E-gun evaporation at  $4 \times 10^{-5}$  Torr to a physical thickness of  $1.0 \mu\text{m}$  on a second set of parts. Adhesion test results are tabulated in Fig. 22.30 for both evaporations; examples of scratches are also shown in Fig. 22.30. Cleaning method (b) produced such superior results that the substrate fractured before the coating was removed. The possibility that the UV ozone treatment creates a reactive surface that enhances adhesion is suggested by the observation that a post-UV ozone treatment alcohol wipe prior to coating did not lower  $W_c$ , whereas the alcohol wipe by itself did not exhibit particularly good results. No useful acoustic signals were detected for this experiment.

SiO on Si (resistance evaporation)  
(physical thickness, 0.37  $\mu\text{m}$ )

|     | Process  | $W_c$ , kg       |
|-----|----------|------------------|
| (a) | Alcohol* | < 0.27           |
| (b) | UV/ozone | > 0.99           |
| (c) | Liquinox | failed tape test |

Ta<sub>2</sub>O<sub>5</sub> on Si (E-gun)  
(physical thickness, 1.0  $\mu\text{m}$ )

|     | Process               | $W_c$ , kg    |
|-----|-----------------------|---------------|
| (a) | Alcohol               | < 0.70        |
| (b) | UV/ozone†             | > 0.95 ± 0.05 |
| (c) | UV/ozone<br>+ Alcohol | > 0.95        |



No Useful Acoustic Signal

G1498

Fig. 22.30

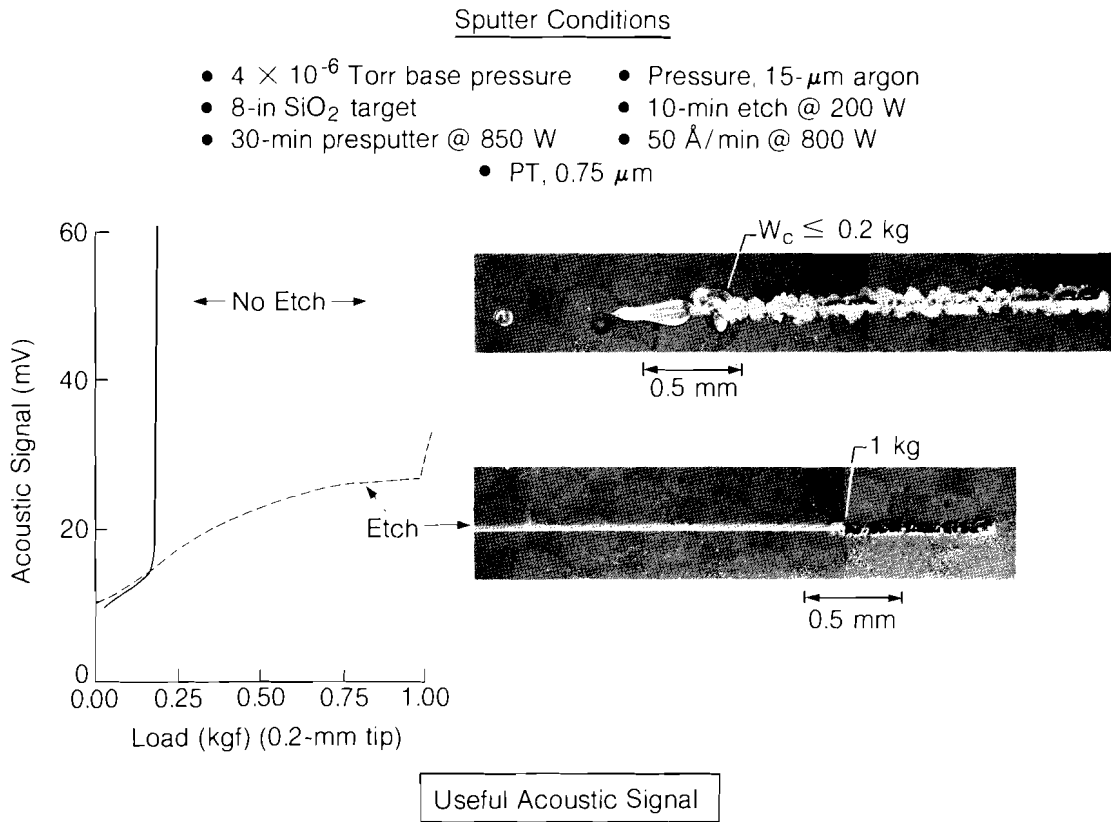
Cleaning experiment 1. A UV-ozone cleaning performed on Si prior to coating deposition greatly improves the adhesion of two separate metal oxides. No useful acoustic signals were measured for this experiment.

### Substrate Cleaning Experiment 2

In this experiment a set of silicon samples was sputter coated using argon and an SiO<sub>2</sub> target with and without a cleaning etch. Coatings were deposited to a physical thickness of 0.75  $\mu\text{m}$ . Additional experimental parameters are given in Fig. 22.31, which also shows the photomicrographs. Excellent acoustic signals were obtained with good reproducibility. The data clearly demonstrate a factor of 5 improvement in adhesion with sputter etching prior to deposition.

### Substrate Cleaning Experiment 3

The versatility of the dynamically loaded scratch tester was demonstrated by evaluating a system consisting of silver, deposited with E-beam evaporation to a physical thickness of 0.10  $\mu\text{m}$ , on a polyethylene film base 0.15-mm thick (see Fig. 22.32). We measured a twenty-fold improvement in adhesion when the substrate was cleaned with a butane-methylene-chloride process. Previous attempts to select an optimum cleaning process for improved adhesion met with no success because all films failed the cellophane-tape pull test.



G1499

Fig. 22.31  
 Cleaning experiment 2. Sputter etching of Si prior to sputter coating improves the adhesion of SiO<sub>2</sub> film by more than a factor of 5. Excellent acoustic signals gave real-time information during this experiment.

Our preliminary survey has shown that the dynamically loaded scratch tester gives relative adhesive strength information for some interesting optical thin-film-substrate systems. Substrate fracture prior to adhesive failure limits the utility of the present device for many other systems of interest, and acoustic emission has been shown to be useful in but a few situations. Future work must attempt to understand the reasons for the limitations imposed upon this apparatus and, if possible, modify the stylus geometry to reduce substrate fracture and enhance acoustic emission signals. The apparatus as presently constructed will enable us to continue our work to relate coating adhesion to processing variables in thin-film coating technology.

**ACKNOWLEDGMENT**

This work was supported by the U.S. Department of Energy Office of Inertial Fusion under agreement number DE-FC08-85DP40200 and by the Laser Fusion Feasibility Project at the Laboratory for Laser Energetics which has the following sponsors: Empire State Electric Energy Research Corporation, General Electric Company, New York State Energy Research and Development Authority, Northeast Utilities Service Company, Ontario Hydro, Southern California Edison Company, The Standard Oil Company, and University of Rochester. This work was also supported in part by the New York State Center for Advanced Optical Technology of the Institute of Optics. Such support does not imply endorsement of the content by any of the above parties.



11. Manual Revetest with Acoustic Emission, manufactured by Laboratoire Suisse de Recherches Horlogères, Rue A-L Breguet 2, CH-2000 Neuchatel, Switzerland.
12. P. Laeng and P. A. Steinmann, *Proceedings of the 8th International Conference on Chemical Vapor Deposition*, Paris, 1981 (Electrochemical Society, Pennington, N.J., 1981) pp. 723–736.
13. A. J. Perry, *Thin Solid Films* **107**, 167–180 (1983).
14. A. J. Perry, *Thin Solid Films* **78**, 77–93 (1981).
15. E. H. Farnum, A. R. Gutacker, and R. Mulford, *J. Vac. Sci. Technol.* **18** (3), 1195–1197 (1981).

### 3.C Characterization of Ultrafast Devices Using Electro-Optic Sampling

Recent advances in GaAs technology have resulted in several new classes of devices, all of which have very high-speed response.<sup>1,2</sup> These devices have been shown to have rise times (10–90% of peak) of tens of picoseconds,<sup>1</sup> which have been measured indirectly.

The indirect measurements are necessary since the fastest commercially available sampling oscilloscope has an intrinsic response time of 25 ps and jitter of a few picoseconds. One way to accomplish this measurement is by the use of a ring oscillator. Here, many devices are connected in serial with the output fed back to the input. The overall rise time of the oscillator is then equal to the rise time of a “typical” device times the number of devices in the ring. While this scheme is easy to implement, the contributions from individual devices are averaged. High-frequency gain measurements, on the other hand, can be made using cw microwave sources. Due to frequency limitations of current packaging techniques, most measurements are limited to 18 GHz.

The electro-optic sampling system<sup>3</sup> developed at LLE has a demonstrated response time of less than half of a picosecond.<sup>4</sup> The corresponding bandwidth extends into the terahertz regime, making this system very attractive for the characterization of individual devices in the picosecond regime.

As shown below, the extreme speed and bandwidth available with this system allow measurements, which yield not only information on the rise time of an individual device, but also its high-frequency gain characteristics, transit time effects, variations of gate capacitance with gate bias, etc. All of these measurements are essential for a complete understanding of these devices.

Descriptions of the sampling system have been published previously.<sup>3,5</sup> In this system, pairs of 100-fs pulses at 615 nm and 100-MHz repetition rate are produced by a colliding-pulse, mode-locked (CPM) laser. One pulse train is used to produce electrical transients via

a Cr-doped GaAs photoconductive switch. This electrical pulse is superimposed onto a dc bias and applied to the gate of the transistor. The inverted and amplified output, superimposed on the drain bias, is then propagated along the electrodes of a LiTaO<sub>3</sub> sampling crystal. This electrical signal induces a change in the optical birefringence of the crystal, and the change is then detected with the second pulse train from the CPM laser and slow-speed photo detectors. A lock-in detection scheme, in which one of the pulse trains is chopped at an audio frequency, along with signal averaging, makes possible millivolt sensitivity for this system.

Two different sampling head geometries, shown in Fig. 22.33, have been used in these experiments. Each offers advantages to the experimenter and points out the variety of geometries available. When designing sampling heads such as these, it is essential that the response of the sampler be faster than that of the device. For devices with response times of tens of picoseconds or less, this means that commercially available connectors, which produce too much dispersion, cannot be used. In fact, the entire structure must be kept as small as possible. This minimizes the path length traveled by the high-speed signal and thus minimizes the dispersion that would otherwise be introduced into the signal.

As shown in Fig. 22.33, the Cr:GaAs switch, the device, and the sampling crystal are all as close to each other as possible. The wire bonds for high-speed input and output are kept as short as possible. In the sampler of Fig. 22.33(a), a three-wire transmission line, consisting of two ground lines and a signal line, was used. This preserved the symmetry of the MESFET geometry itself, since the two source terminals are both grounded. The geometry of the GaAs switch was chosen to allow for direct biasing of the gate of the device while keeping the actual switch as close as possible.

Figure 22.33(b) shows a schematic of the TEGFET [two-dimensional electron gas field transistor, also known as high-electron mobility transistor (HEMT), or modulation-doped field effect transistor (MODFET)] sampling head. The microstrip sampling crystal was chosen for its very high-speed response due to its very small height. Gate biasing for the TEGFET was accomplished by a very long wire bonded directly to the gate pad. The high inductance of this connection preserved the signal shape produced by the conventional microstrip GaAs switch. To date, both MESFET's (metal semiconductor field effect transistors) and TEGFET's have been tested. The MESFET response time was 25 ps, which agrees with S-parameter measurements, and the TEGFET response time of 16 ps agreed with the calculated cutoff frequency.

The experimental results shown in Fig. 22.34 demonstrate some of the measurements that can be made with the electro-optic sampling system. Figure 22.34(a) shows the TEGFET outputs for the device in the "on" and "off," or pinchoff, states. In Fig. 22.34(b) the MESFET response is shown with and without applied drain bias. Note that in all the experimental results shown, the input signal, which is capacitively coupled through the device, appears as a small negative going precursor to the

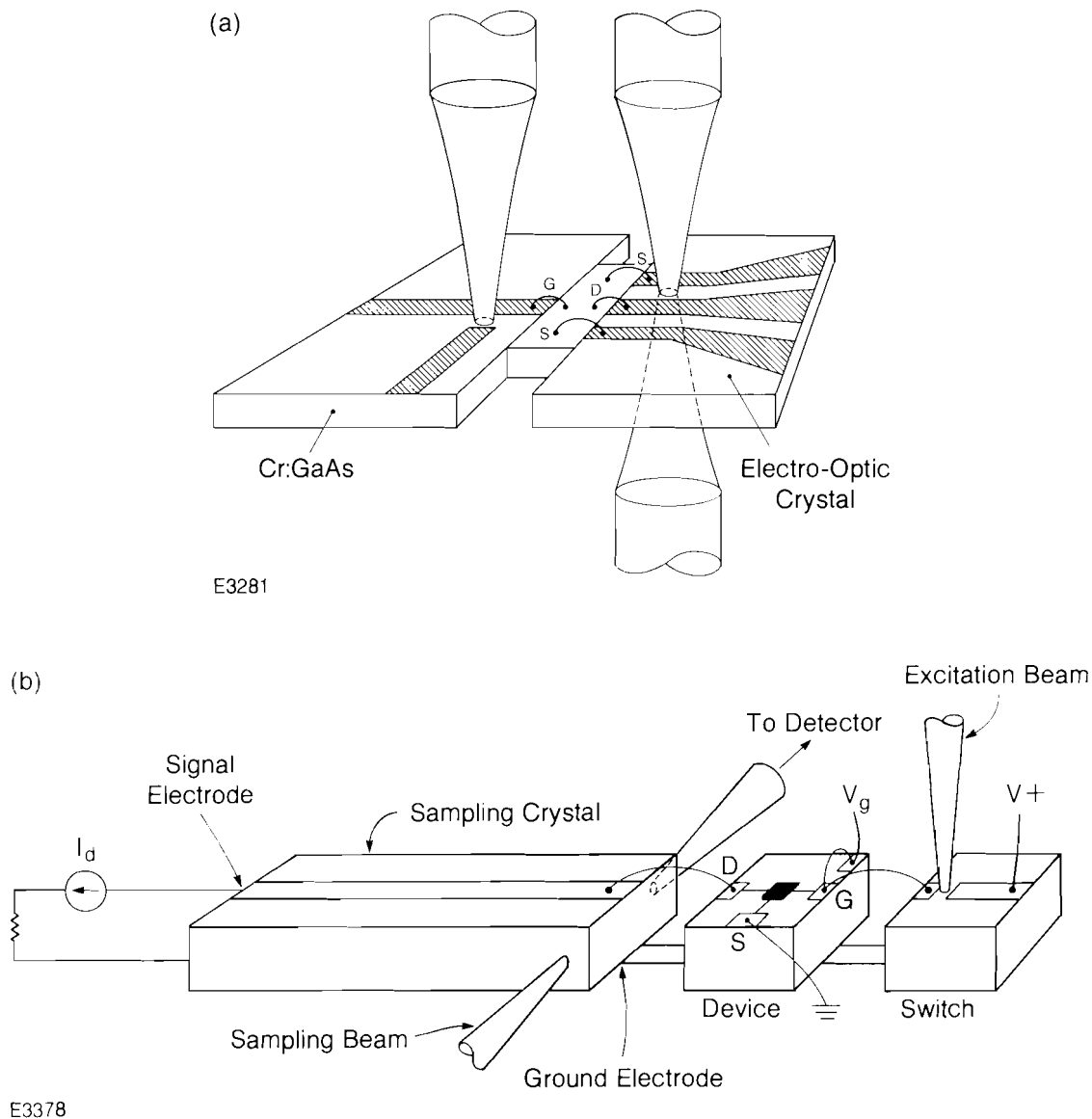


Fig. 22.33  
 Experimental sampling geometries used to characterize high-speed devices. (a) MESFET geometry uses photoconductive switch at right angle to gate bias line. Three-conductor transmission line on sampling crystal preserves symmetry introduced by device geometry. Flared conductors at far end of crystal preserve impedance and prevent reflections of electrical signals, while allowing sufficient width of the conductors for proper termination. (b) TEGFET sampling head uses all microstrip geometry to insure high-speed response equal to that of the device. All connections to and from the sampler were made with wire bonds. High-speed connections from photoconductive switch to the device, and from device to sampling crystal, were as short and as flat as possible in order to minimize deviations from proper high-speed transmission-line behavior. Bias lines were bonded in large vertical loops, whose large inductance would prevent degradation to the high-speed signals.

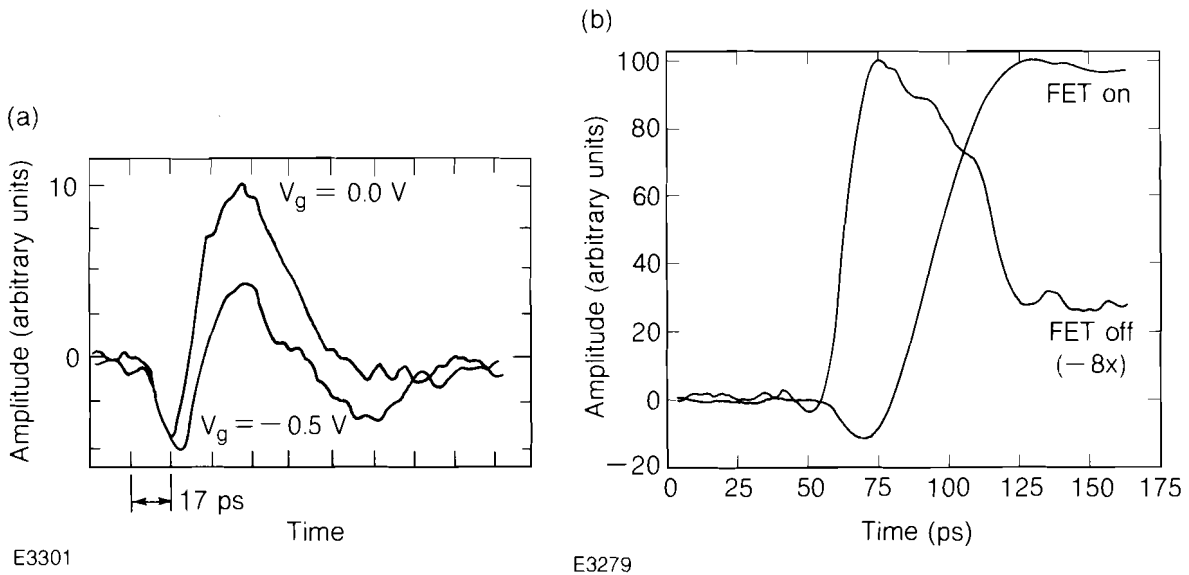


Fig. 22.34

(a) MESFET response measured with and without applied drain bias. Note that without applied bias (FET off), the curve is magnified eight times and inverted. This type of measurement yields information on transit time effects as well as rise times. (b) TEGFET response measured in the "on" (conducting,  $V_g = 0.0 \text{ V}$ ) and "off" (pinch-off,  $V_g = -0.5 \text{ V}$ ) states. Information on gate capacitance as well as rise times are obtained in this way.

main output. This new result, only achievable using the electro-optic sampler, now makes possible measurements of the device characteristics that only become important in the picosecond regime. In the case of TEGFET's, it is known that these devices are even faster when operated in a  $77^\circ\text{K}$  environment.<sup>1</sup> This increased performance is because the electron gas experiences less scattering from the cold GaAs lattice (phonons). To extend the operating range of the sampler to this regime, a cryo-sampler is being developed. The initial version of this sampler had a response time of  $16.4 \text{ ps}$  at  $4.2^\circ\text{K}$ .<sup>6</sup> This response time was limited by needing long, dispersive cables to conduct the electrical transient from the room temperature to the cryogenic environment. By modifying the cryo-sampler to operate directly at lower, cryogenic temperatures, we have extended the operating regime of the electro-optic sampling system to encompass not only the range of two-dimensional electron gas device environments, but the entire class of superconducting devices as well.

Superconducting devices offer the potential of both very high-speed and very low-power dissipation. An all-superconducting sampler has recently been demonstrated with a  $2.1\text{-ps}$  response time.<sup>7</sup> Microwatt supercomputer logic subsystems have been designed and tested.<sup>8,9</sup> Novel superconducting devices, such as QUITERON<sup>10</sup> and SMEFET,<sup>11</sup> offer the potential for even faster response times. The current version of the cryo-sampler has demonstrated a room-temperature response time

of 1 ps. When operating at 4.2°K, the reduced dispersion of the superconducting transmission line, which connects the photoconductive switch and sampler, is expected to reduce the response time even further.

Another application of the electro-optic sampling system involves using an electrodeless sampling crystal in a reflection mode geometry, to allow access to an otherwise remote device. This geometry, reported previously, has a demonstrated response time of 0.75 ps.<sup>12</sup> In this technique, the optical birefringence is induced by the fringing electric field, thus eliminating the need for electrical connections between the sampling crystal and the circuit being characterized. This approach is especially attractive for more mature technologies, where more than a few devices are fabricated on a single wafer or substrate, making it impractical to allow for direct characterization of individual devices. Reflection mode sampling is currently under investigation for characterizing high-speed planar microwave structures.

#### ACKNOWLEDGMENT

This work was supported by the following sponsors of the Laser Fusion Feasibility Project at the Laboratory for Laser Energetics—Empire State Electric Energy Research Corporation, General Electric Company, New York State Energy Research and Development Authority, Northeast Utilities Service Company, Ontario Hydro, Southern California Edison Company, The Standard Oil Company, and University of Rochester. Such support does not imply endorsement of the content by any of the above parties.

#### REFERENCES

1. H. Morkoc and P. M. Solomon, *IEEE Spectrum* **21** (2), 28 (1984).
2. G. H. Döhler, *Sci. Am.* **249** (5), 144 (1984).
3. J. A. Valdmanis, G. Mourou, and C. W. Gabel, *Appl. Phys. Lett.* **41**, 211 (1982).
4. G.A. Mourou and K. E. Meyer, *Appl. Phys. Lett.* **45**, 492 (1984).
5. J. A. Valdmanis, G. A. Mourou, and C. W. Gabel, *IEEE J. Quantum Electron.* **QE-19**, 664 (1983).
6. D. R. Dykaar, T. Y. Hsiang, and G. A. Mourou, *IEEE Trans. Magn.* **MAG-21** (2), 232 (1985).
7. P. Wolf and B. J. Van Zeghbroeck, Proceedings of the Applied Superconductivity Conference (1984), p. 10.
8. W. Anacker, *IBM J. Res. Dev.* **24** (2), 107 (1980).
9. A. Mukherjee, *Elec. Dev. Lett.* **3** (2), 29 (1982).
10. S. M. Faris, S. I. Raider, W. J. Gallagher, and R. E. Drake, *IEEE Trans. Magn.* **MAG-19**, 1293 (1983).
11. T. Y. Hsiang and A. M. Goldman, Superconducting Magneto-Electric Field Effect Transistor (U.S. patent application).
12. K. E. Meyer and G. A. Mourou, *Electron. Lett.* (submitted February 1985).

## Section 4

# NATIONAL LASER USERS FACILITY NEWS

This report covers the activities of the National Laser Users Facility during the quarter 1 January to 31 March 1985. During this period two users visited LLE to discuss their experiments.

On 4 March 1985, the National Laser Users Facility Steering Committee held its sixth annual meeting to review and approve proposals and to recommend funding of approved proposals in inertial fusion to the U.S. Department of Energy. This funding allocation is separate from LLE's operation contract and is designed to provide research funds to users in the inertial fusion field. Users in other fields may use the facility but must provide their own research funds.

Eighteen proposals were submitted to the committee this year. The proposals were in a variety of areas, including plasma physics, x-ray laser research, x-ray spectroscopy, instrumentation, nuclear fluorescence, materials research, and atomic physics. Nine of the eighteen were recommended for approval. This year three new user experiments were approved for facility time. These new proposals represent a third of the total approved number. Individual funding levels for these experiments were recommended to the Department of Energy for their consideration. An upcoming issue of the LLE Review will highlight the approved proposals.

Further information on the National Laser Users Facility is available from:

Thomas C. Bristow, Manager  
National Laser Users Facility  
Laboratory for Laser Energetics  
University of Rochester  
250 East River Road  
Rochester, New York 14623-1299  
(716) 275-2074

ACKNOWLEDGMENT

This work was supported by the U.S. Department of Energy Office of Inertial Fusion under agreement number DE-FC08-85DP40200 and the various contracts awarded users of the National Laser Users Facility.

# PUBLICATIONS AND CONFERENCE PRESENTATIONS

## Publications

G. Mourou, W. H. Knox, and S. Williamson, "High-Power Picosecond Switching in Bulk Semiconductors," in *Picosecond Optoelectronic Devices*, edited by Chi H. Lee (Academic Press, New York, 1984), pp. 219–248.

C. A. Hanzlik, W. H. Knox, T. M. Nordlund, R. Hilf, and S. L. Gibson, "Picosecond Fluorescence of Hematoporphyrin Derivative, Its Components and Related Porphyrins," in *Porphyrin Localization and Treatment of Tumors*, edited by D. R. Doiron and C. J. Gomer (Alan R. Liss, New York, 1984), pp. 201–210.

L. P. Forsley, "A Review of RISC and Forth Machine Literature," *The Journal of Forth Application and Research* 2(1), 85–88 (1984).

Robert D. Frankel and James M. Forsyth, "Time-Resolved X-Ray Diffraction Study of Photostimulated Purple Membrane," *Biophys. J.* 47, 387–393 (1985).

## Forthcoming Publications

I. N. Duling III, T. Norris, T. Sizer II, P. Bado, and G. Mourou, "Kilohertz Synchronous Amplification of 85-fs Optical Pulses," accepted for publication in the *Journal of the Optical Society of America*.

T. Norris, T. Sizer II, and G. Mourou, "Generation of 85-fs Pulses by Synchronous Pumping of a CPM Dye Laser," accepted for publication in the *Journal of the Optical Society of America*.

W. E. Behring, J. F. Seely, S. Goldsmith, L. Cohen, M. C. Richardson, and V. Feldman, "Transitions of the Type 2s-2p in Highly Ionized Zn, Ga, and Ge," accepted for publication by the *Journal of the Optical Society of America*.

M. C. Richardson, R. S. Craxton, J. Delettrez, R. L. McCrory, W. Seka, and J. M. Soures, "Absorption Physics at 351 nm in Spherical Geometry," to be published in *Physical Review Letters*.

N. Delameter, C. F. Hooper, R. F. Joyce, L. A. Woltz, N. M. Ceglio, R. L. Kaufmann, R. W. Lee, and M. C. Richardson, "Opacity Effects on H-Like X-Ray Lines Emitted from Laser Driven Implosions," to be published in *Physical Review A*.

F. Guglielmi, "Fabrication of Polymeric Microballoons for Ablative Inertial Fusion Targets," accepted for publication in the *Journal of Vacuum Science and Technology A*.

V. Feldman, J. F. Seeley, M. C. Richardson, W. E. Behring, and S. Goldsmith, "Transitions of the Type 2s-2p in Fluorine-Like and Oxygen-Like As, Se, Br and Rb<sup>x</sup>," to be published in the *Journal of the Optical Society of America B*.

H. Kim and M. D. Wittman, "X-Ray Microradiography of Inertial Fusion Targets Using a Laser Produced Plasma as an X-Ray Source," accepted for publication in the *Journal of Vacuum Science and Technology A*.

S. G. Noyes and H. Kim, "Aluminum/Aluminum-Nitride Sputter Deposition on the Inertial Fusion Target Using the Pulsed-Gas Process," accepted for publication in the *Journal of Vacuum Science and Technology A*.

S. Williamson, G. Mourou, and J. C. M. Li, "Time-Resolved Laser-Induced Phase Transformation in Aluminum" to be published in the *Proceedings of MRS Symposium on Energy Beam-Solid Interactions and Transient Thermal Processing*.

K. A. Tanaka, B. Boswell, R. S. Craxton, L. M. Goldman, F. Guglielmi, W. Seka, R. W. Short, and J. M. Soures, "Brillouin Scattering, Two-Plasmon Decay, and Self-Focusing in Underdense UV Laser-Produced Plasmas," accepted for publication in *Physics of Fluids*.

F. Guglielmi, "Low Density Foam for Self-Focusing Inertial Fusion Targets," accepted for publication in the *Journal of Vacuum Science and Technology A*.

J. F. Seeley, C. M. Brown, V. Feldman, M. Richardson, B. Yaakobi, and W. E. Behring, "Evidence for Lasing on the 182-Å Transition of CVI in a Radiation-Cooled Plasma," to be published in *Optics Communications*.

B. Yaakobi, O. Barnouin, J. Delettrez, L. M. Goldman, R. Marjoribanks, R. L. McCrory, M. C. Richardson, and J. M. Soures, "Thermal Transport Measurements in Six-Beam, UV Irradiation of Spherical Targets," accepted for publication in the *Journal of Applied Physics*.

B. A. Brinker, "Microradiographic Self-Imaging of DT-Filled Inertial Fusion Targets," accepted for publication in the *Journal of Vacuum Science and Technology*.

B. Yaakobi, R. D. Frankel, J. M. Forsyth, and J. M. Soures, "Laser Generated X-Ray Source for Time-Resolved Biological and Material Structure Studies," to be published by Academic Press.

## Conference Presentations

A. Simon, "New Model of Raman Spectra in Laser-Produced Plasma," presented at the Meeting of the American Physical Society, Toronto, Ontario, January 1985.

P. Bado, I. N. Duling III, T. Sizer II, T. B. Norris, and G. A. Mourou, "Generation of White Light at 1 kHz," presented at the SPIE Conference on Ultrashort Pulse Spectroscopy and Applications, Los Angeles, CA, January 1985.

---

The following presentations were made at the Fifth Topical Conference on Atomic Processes in High-Temperature Plasmas, Pacific Grove, CA, February 1985:

O. Barnouin, R. S. Marjoribanks, M. C. Richardson, B. Yaakobi, S. R. Goldman, P. D. Goldstone, A. Hauer, W. C. Mead, P. A. Jaanimagi, and B. L. Henke, "M-Line Spectra from UV-Laser-Irradiated High-Z Plasmas."

R. Epstein, S. Skupsky, and B. Yaakobi, "Absorption Spectroscopy as a Density Diagnostic for Dense Imploded Shells."

R. S. Marjoribanks, M. C. Richardson, R. Epstein, P. A. Jaanimagi, J. Delettrez, and O. Barnouin, "Characterization of the Temperature Profile from the Ionization Front in Laser Plasma Interactions."

M. C. Richardson, O. Barnouin, R. Epstein, R. S. Marjoribanks, J. M. Soures, B. Yaakobi, P. A. Jaanimagi, and B. L. Henke, "Characteristics of Laser-Imploded Cylindrical Plasmas."

J. F. Seeley, V. Feldman, C. M. Brown, M. C. Richardson, B. Yaakobi, and W. E. Behring, "Evidence for Lasing Action on the CVI 182-Å Transition in a Radiation-Cooled Plasma."

---

The following presentations were made at the Topical Meeting on Picosecond Electronics and Opto-Electronics, Incline Village, NV, March 1985:

D. R. Dykaar, T. Y. Hsiang, and G. A. Mourou, "Development of a Picosecond Cryo-Sampler Using Electro-Optic Techniques."

C. J. Kryzak, S. M. Faris, K. E. Meyer, and G. A. Mourou, "Transmission Line Designs with a Measured Step Response of 3 ps per Centimeter."

K. E. Meyer, D. R. Dykaar, and G. A. Mourou, "Characterization of TEGFET's and MESFET's Using the Electro-Optic Sampling Technique."

K. E. Meyer and G. A. Mourou, "Two-Dimensional E-Field Mapping with Subpicosecond Resolution."

S. Williamson and G. Mourou, "Picosecond Electro-Electron Optic Oscilloscope."

---

The following presentations were made at the Fourth Target Specialists Meeting at St. Petersburg, FL, March 1985:

H. Kim and J. M. Soures, "Inertial Confinement Fusion Target Fabrication Activities at the Laboratory for Laser Energetics, University of Rochester."

H. Kim, S. Noyes, and M. C. Richardson, "Fabrication of Thin Film Cylindrical Targets for X-Ray Laser Experiments."

The work described in this volume includes current research at the Laboratory for Laser Energetics which is supported by Empire State Electric Energy Research Corporation, General Electric Company, New York State Energy Research and Development Authority, Northeast Utilities Service Company, Ontario Hydro, Southern California Edison Company, The Standard Oil Company, University of Rochester, and the U.S. Department of Energy Office of Inertial Fusion under agreement DE-FC08-85DP40200.

